Doppler Velocimetry Using Fabry-Perot Imaging

by

Magnus Lipp
Research Department

JANUARY 2001

**NAVAL AIR WARFARE CENTER WEAPONS DIVISION
CHINA LAKE, CA 93555-6100**

20010220 056

Naval Air Warfare Center Weapons Division

FOREWORD

This report documents work carried out and completed during an American Society of Engineering Education (ASEE) postdoctoral fellowship, starting 15 March 1999. The research resulted in a radiometric assessment of the potential usefulness of naturally occurring spectral line sources for passive Fabry-Perot Doppler velocimetry imaging and a quantitative evaluation tool of different laser sources with regard to different velocity regimes for active illumination.

This report was reviewed for technical accuracy by C. D. Marrs and Lewis DeSandre.

REPORT DOCUMENTATION PAGE

Public reporting burden for this collection of information is estimated to average 1 hour per response, including the time for reviewing instructions, searching existing data sources, gathering and maintaining the data needed, and completing and reviewing the collection of information. Send comments regarding this burden estimate or any other aspect of this collection of information, including suggestions for reducing this burden, to Washington Headquarters Services, Directorate for Information Operations and Reports, 1215 Jefferson Davis Highway, Suite 1204, Arlington, VA 22202-4302, and to the Office of Management and Budget, Paperwork Reduction Project (0704-0188), Washington, DC 20503.

1. AGENCY USE ONLY (Leave blank)	2. REPORT DATE January 2001	3. REPORT TYPE AND DATES COVERED Final, FY99

4. TITLE AND SUBTITLE
Doppler Velocimetry Using Fabry-Perot Imaging (U)

5. FUNDING NUMBERS

6. AUTHOR(S)

Magnus Lipp

7. PERFORMING ORGANIZATION NAME(S) AND ADDRESS(ES)

Naval Air Warfare Center Weapons Division
China Lake, CA 93555-6100

8. PERFORMING ORGANIZATION REPORT NUMBER

NAWCWD TP 8459

9. SPONSORING/MONITORING AGENCY NAME(S) AND ADDRESS(ES)

American Society for Engineering Education
1818 N. Strteet, N.W.
Suite 600
Washington, DC 20036

10. SPONSORING/MONITORING AGENCY REPORT NUMBER

11. SUPPLEMENTARY NOTES

12A. DISTRIBUTION/AVAILABILITY STATEMENT

A Statement; public release; distribution unlimited.

12B. DISTRIBUTION CODE

13. ABSTRACT   *(Maximum 200 words)*

(U) The feasibility of measuring velocities of potentially multiple objects via the Doppler effect using Fabry-Perot imaging has been explored. This report consists of two parts: an experimental, active approach where the target scene is illuminated by a multimode Ar-ion laser; and a passive approach assessing the possibility of using naturally occuring spectrally narrow lines for illumination. For the experimental approach it was found that it is advantageous to use multimode lasers with narrow longitudinal mode spacing, especially for the lower velocity regime. If the cavity length is chosen to be an integer multiple of the Fabry-Perot plate distance, a dense interference ring pattern results and overlapping of stationary and dynamic ring parts occurs at already low speeds of tens of m/s. The light intensity provided by laser illumination is compared to the intensity of the brightest natural line source in the atmosphere, the OH-Meinel bands. The most intense ones of these are emitted from vibrational transitions of the OH molecule between 1.5- and 1.8-μm wavelength. Because they are generated in the coldest atmospheric layer (-90° C), about 90 km above ground, the Doppler linewidth is the smallest available, promising also the best resolution.

14. SUBJECT TERMS
Doppler Velocimetry, Fabry-Perot Imaging, Airglow, OH-Meinel Bands

15. NUMBER OF PAGES
46

16. PRICE CODE

17. SECURITY CLASSIFICATION OF REPORT	18. SECURITY CLASSIFICATION OF THIS PAGE	19. SECURITY CLASSIFICATION OF ABSTRACT	20. LIMITATION OF ABSTRACT
UNCLASSIFIED	UNCLASSIFIED	UNCLASSIFIED	UL

CONTENTS

———

INTRODUCTION

The goal of this fiscal year 1999 project was to detect and measure the velocities of multiple objects approaching the observer through Fabry-Perot filter Doppler imaging. The possible advantages are to discover approaching objects that are otherwise lost in noisy environments and/or background clutter and to provide the observer with velocity data—especially for high speed—while maintaining the imaging. If successful, the passive part of this project might even allow doing this without a laser or other man-made light source. The Fabry-Perot itself could be a rather simple and inexpensive part of the system in principle and might just be a solid semitransparent etalon.

DOPPLER EFFECT (BACKGROUND)

The general geometry for the Doppler effect is shown in Figure 1.
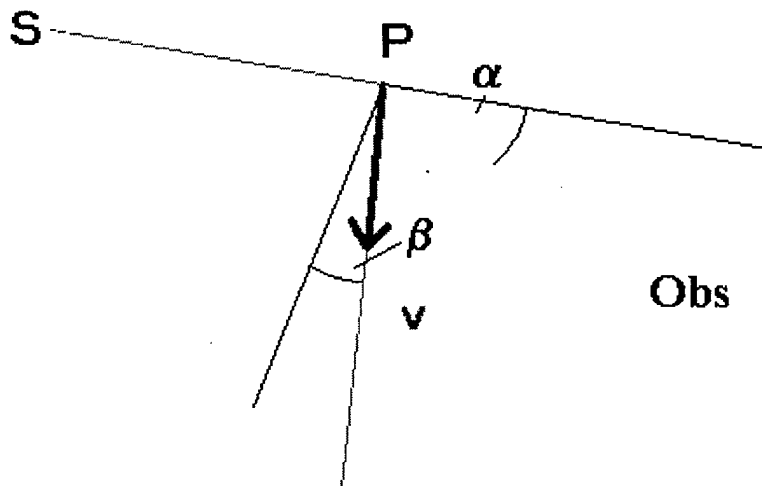
FIGURE 1. General Geometry for the Doppler Effect. S: source of the light; P: object moving in direction of velocity v; Obs: observer; α: scattering angle; β: angle between the direction v and the line bisecting the angle included between S and the observer Obs.

The fractional frequency shift is found by calculating

$$\Delta v/v \cong 2v/c \, \cos(\beta) \, \sin(\alpha/2)$$

Figure 2 shows the ideal geometry (i.e., β close to 0 degree and α close to 180 degrees). In that case the fractional frequency shift is about twice the ratio of the velocity to the speed of light.
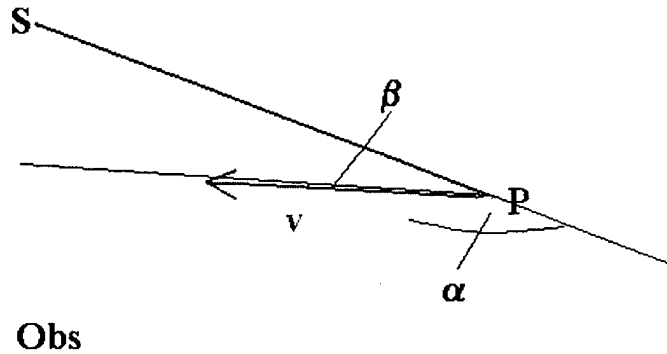
FIGURE 2. Geometry Close to the Ideal: α is Close to 180 Degrees and β is Almost 0 Degree.

Table 1 demonstrates the magnitude of the effects in the visible. The values were calculated based on $\Delta v/v \cong v/c$, so the effect could be twice as much in the ideal case.

TABLE 1. Doppler Shifts for Different Wavelengths and Velocities Based on $\Delta v/v \cong v/c$.

Velocity			Doppler shift (MHz) at $\lambda=488$ nm (blue) [$6.15 \cdot 10^{14}$ Hz]	Doppler shift (MHz) at $\lambda=633$ nm (red) [$4.74 \cdot 10^{14}$ Hz]
(m/s)	(mph)	(km/h)		
10	22.5	36	20.5	15.8
20	44.4	72	41.0	31.6
30	67.5	108	61.5	47.4
50	112.5	180	102.5	79.0
80	180	288	164	126.4
100	225	360	205	158
300	675	1080	615	474
500	1125	1800	1025	790

Comparing the Doppler shifts with the frequencies one finds that the effects are on the order of 0.03 ppm (10 m/s) to 1 ppm (300 m/s).

FABRY-PEROT (BACKGROUND)

The Fabry-Perot imaging technique has been employed previously when measuring velocities of energetic materials after ignition or windspeeds in the upper atmosphere (References 1 through 3). The Fabry-Perot (homodyne measurement) is chosen because it has the highest optical throughput when compared with other interferometric devices and because high velocities cannot be determined by heterodyne techniques (Reference 1). The Fabry-Perot itself is—in its simplest form—a pair of plane parallel semitransparent mirrors that introduces phase shifts between the reflected branches of a lightbeam entering the device under an angle θ with the optical axis (figure axis) of the system (see Figure 3).
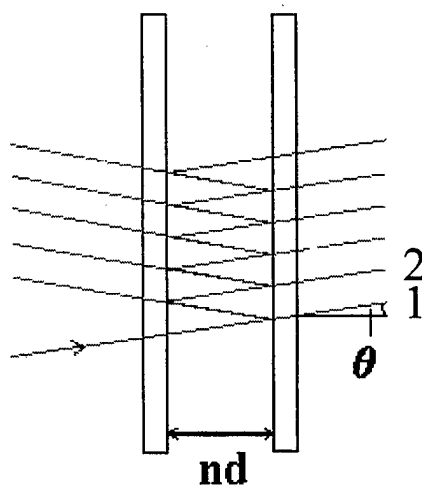
FIGURE 3. Schematic of a Fabry-Perot With Distance d Between the Plates. If the space between the plates is filled by a medium with index of refraction n, the optical path will be nd. The light beam enters the system from the left under an angle θ to the optical axis.

The path difference s between beams 1 and 2 is exactly

$$s = 2\, nd \cos \theta$$

The refraction of the beams inside the plates is included. Constructive interference is obtained when $s = m\lambda$ and the interference pattern to the right of the plates is a set of concentric circles. The highest interference order is obtained for the smallest angle θ. If there is a maximum in the center ($\theta = 0$), then the maximum interference order is

$$m_{max} = 2\ nd\ /\ \lambda$$

Figure 4 shows the interference pattern obtained when there is constructive interference at the center.
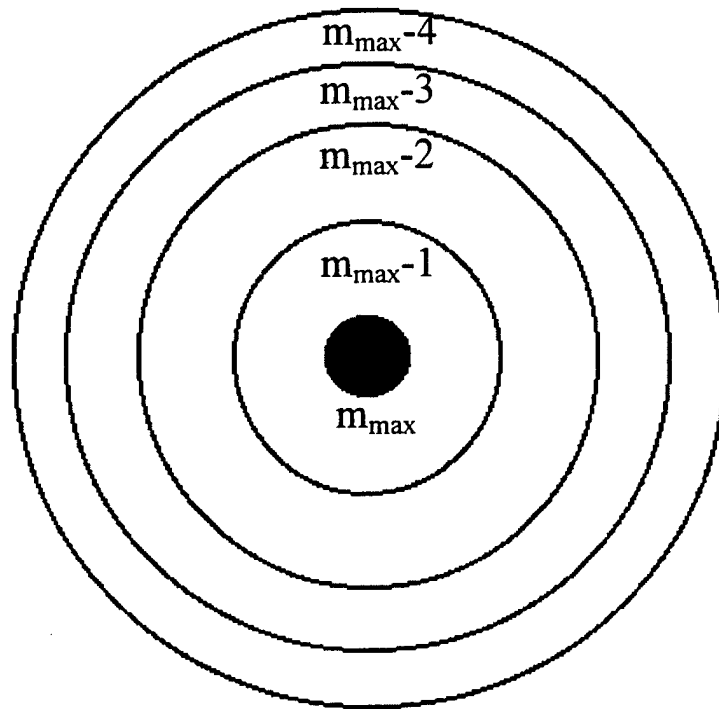
FIGURE 4. "Bulls-Eye" Pattern of a Fabry-Perot When Illuminated by a Monochromatic Laser With ONE Longitudinal Mode.

The radius r_k of fringe circle k is proportional to $\sin\theta_k$. With k running from 0, 1, and 2.... we have

$$r_k \sim \sin\theta_k = \sqrt{1 - \left[\frac{(m_{max} - k)\lambda}{2\ nd}\right]^2}$$

and because $m_{max} \cdot \lambda/2 \, nd = 1$ and $k \cdot \lambda/2 \, nd \ll 1$ we see that

$$r_k \sim \sin\theta_k \approx \sqrt{\frac{k\lambda}{nd}}$$

The current discussion covers two approaches: an active approach using laser radiation as the illumination source (mainly experimental using the available equipment at the Naval Air Warfare Center Weapons Division, China Lake, California) and a passive approach that explored the feasibility of using narrow lines of the airglow in the night sky. These lines would serve as the illumination source for the process. Both active and passive approaches are very similar to each other. The specific difference is the source of illumination:

Active Approach: a narrow linewidth laser (several longitudinal modes are acceptable, maybe even desired, as long as the individual modes are very narrow, on the order of < 100 MHz).

Passive Approach: natural sources of spectral lines in the environment that also exhibit narrow linewidth.

The passive approach started with the attempt to identify suitable spectral lines in the airglow. Because the background during the day is so much higher than at night, the focus was directed at naturally occurring spectral lines of the nightglow. Most of the intensity units in the literature for these extended natural sources are either given in Rayleigh (R) with

$$1R = 10^{10} / 4\pi \text{ photons}/(\text{s m}^2 \text{ sterad})$$

or just in number of photons:

$$N/(\text{s m}^2 \text{ arcsec}^2)$$

The conversion ratio is

$$1kR = 18.7 \text{ photons}/(\text{s m}^2 \text{ arcsec}^2)$$

Actual spectral intensities in the literature are given per wavelength or wave number interval, and therefore the total strength of a line has to be found by spectrally integrating.

A rough estimate can be obtained by simply multiplying the value in R/A or R/cm^{-1} with the spectral width of the recording instrument (resolution).

It should be noted that the airglow is not a constant source with time and homogeneous over the sky but rather patchy and temporally changing (on the time scale of minutes).

ACTIVE APPROACH

Figure 5 is the schematic of the present setup. Maximum power output of the air-cooled Ar-ion laser is about 45 mW in current mode at the 488-nm line. In the specific case tested in the laboratory, the illuminated target is a rotating wheel. The power available for illumination has probably dropped by a factor of 2 due to the reflection losses at the mirrors and lens. The size of the illuminated area is on the order of 1 cm^2.
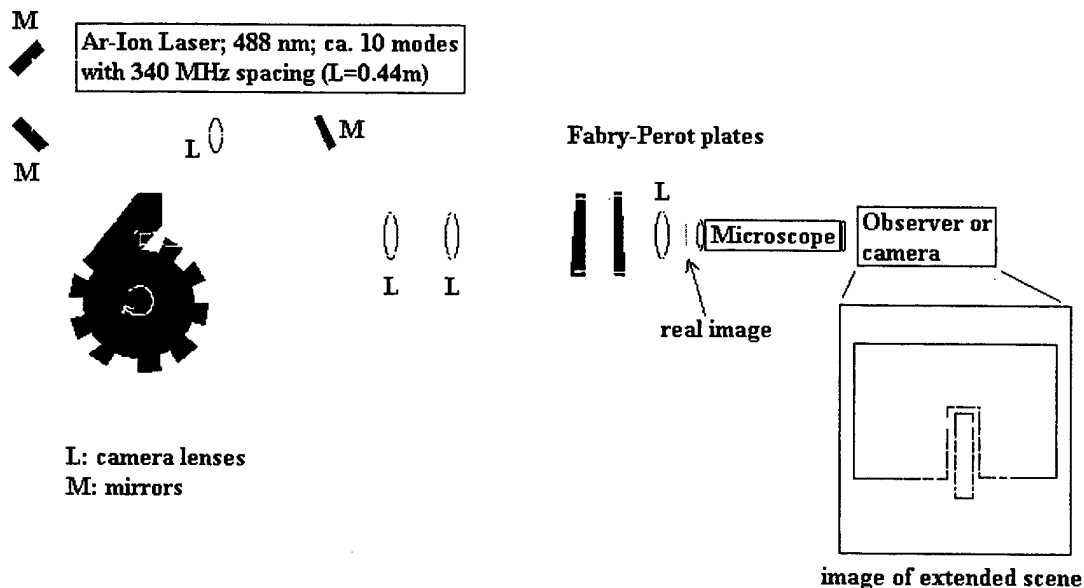
FIGURE 5. Current Experimental Setup. After illumination of the scene, the lenses are camera lenses with F/#'s of 2.5 and 2.8 with focal lengths of 28 and 135 mm before the FP, and F/# of 2.5 and f = 90 mm after the FP. The microscope magnifies by 20 (objective) x 10 (eyepiece). The reflecting parts of the rotating toothed wheel were painted with white diffusely reflecting paint.

The actual fringe pattern is somewhat more complicated than the one described in the introduction because we have multiple (e.g., 10) longitudinal modes, not just one. Each of these modes generates its own fringe pattern. Therefore the fringe circles are NOT

depended on the order k of the ring only, but mainly on the mode spacing 1/2L (in wave numbers) of the laser with cavity length L. A special case exists when the distance d between plates is related to the cavity length L of the laser by an integer number p : then the mode pattern is simple again and good fringe contrast is obtained (References 2 and 4). This is illustrated in the following paragraphs.

Example. The currently used Ar-ion with L= 0.44 m has 10 modes with a longitudinal mode spacing of ca. 340.9 MHz or 0.01136 cm^{-1} (1/2L). If one chooses p = 5 then the plate distance is d = 0.4400 m/5 = 8.800 cm.

Each of the 10 modes has its own fringe pattern. If the shortest wavelength mode is denoted as 0 and the next modes separated from each other by 1/2L are called 1, 2..., then mode 5 will cause constructive interference in the center again, mode 6 will generate the same fringe ring as mode 1 and so on. The complete mode pattern is shown in Figure 6. Table 2 demonstrates this concept numerically. Even though the wavelengths are very close to the actual wavelength of the 488-nm Ar-ion line, they are only used to demonstrate this concept and should NOT be mistaken for true wavelengths of the individual modes.
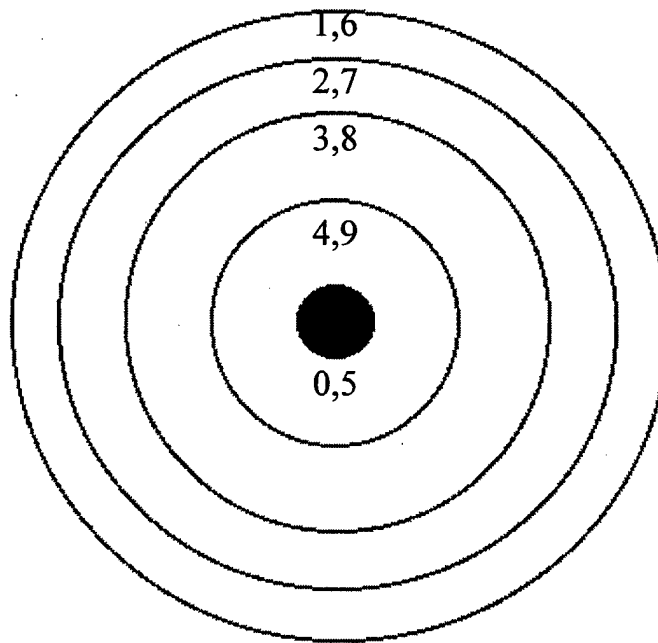
(a) The numbers refer to the 10 different longitudinal modes starting from 0.

FIGURE 6. Complete Mode Pattern Similar.
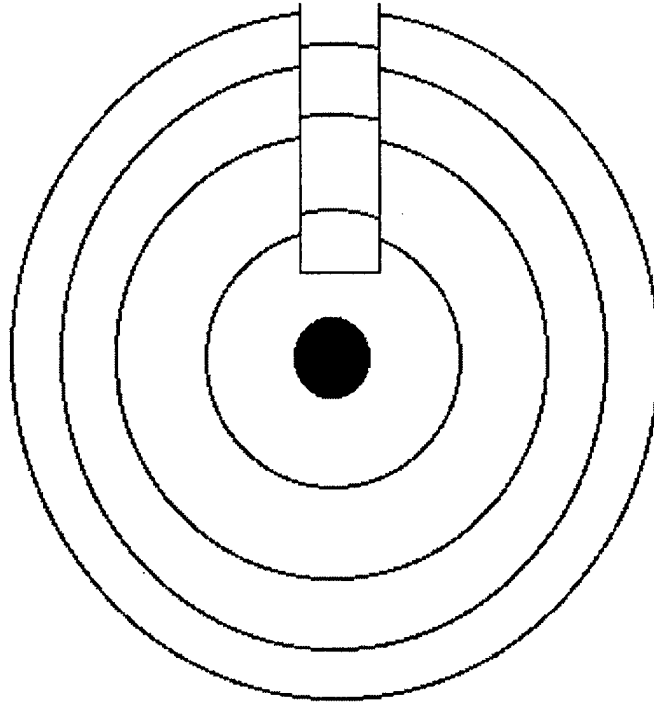
(b) The rectangular object to the top of the center (e.g., a rotating blade) is moving toward the observer, and the fringe circles are displaced outward.

FIGURE 6. Contd.

TABLE 2. Wavelengths of the 10 Modes and Their Fringe Positions. Per "Fabry-Perot" ring (called center, first ring, second ring, and so on) there are 5 "sub-rings" from the 10 laser modes. Each of these sub-rings is made up from 2 modes. The wavelength values are chosen so that they demonstrate the concept; they should not be mistaken for the true wavelengths. But they come very close to the 488-nm line of the Ar-ion laser.

Mode-number q	λ/nm	m_{max} (center)	m_1	$\sin\theta_1/10^{-3}$ (first ring)	m_2	$\sin\theta_2/10^{-3}$ (second ring)
0	488.0009982	360655.0	360654	2.35	360653	3.33
1	488.0012690	360654.8	360654	2.11	360653	3.16
2	488.0015397	360654.6	360654	1.82	360653	2.98
3	488.00181	360654.4	360654	1.49	360653	2.79
4	488.00208	360654.2	360654	1.05	360653	2.58
5	488.00235	360654.0	360653	2.35	360652	3.33
6	488.00262	360653.8	360653	2.11	360652	3.16
7	488.00289	360653.6	360653	1.82	360652	2.98
8	488.00316	360653.4	360653	1.49	360652	2.79
9	488.00343	360653.2	360653	1.05	360652	2.58

Now consider imaging a moving object through the Fabry-Perot. If the observed scene contains a moving object with motion towards the observer, then the fringe pattern will show a discontinuity at the place of the object because the wavelength received by the observer has changed and with it the radius of the fringe.

When the object moves toward the observer, the received wavelength

$$\lambda_v = \lambda \cdot \left(1 - \frac{v}{c}\right)$$

is blue-shifted and the fringes generated by that particular part of the image are displaced outwardly. Looking at the formula earlier, this might seem counter intuitive but this formula only gives the fringe radius for one particular wavelength pattern. It is necessary to look at the Fabry-Perot condition, $m\lambda = 2\,nd\cos\theta$, to give the answer: with m constant and λ decreasing, $\cos\theta$ also has to become smaller which means $\sin\theta$, which is proportional to the radius, becomes larger.

This can also be understood by looking at Table 2. With increasing wavelength the fringes of the laser modes move toward the center (modes 1-5 and 6-9), i.e., with decreasing wavelength they move outward.

These Doppler-shifted parts of the fringes are readily observed in the experiment. One way then to characterize the system described above is by the velocity $v_{overlap}$ required for one of the displaced fringe parts to overlap with the $v = 0$ position of the next ring out.

Example. Necessary velocity for the dynamic ring caused by wavelength λ_4 (λ_9) to overlap with the ring stemming from wavelength λ_3 (λ_8) (at rest) is equal to the mode spacing of the laser divided by the actual energy of the photons in wave numbers multiplied with the speed of light:

$$\sqrt{1 - \left((m_0 - 1) \cdot \lambda_4 / 2d\right)^2 \left(1 - \frac{v_{overlap}}{c}\right)^2} = \sqrt{1 - \left((m_0 - 1) \cdot \lambda_3 / 2d\right)^2}$$

and

$$\frac{v_{overlap}}{c} = 1 - \frac{\lambda_3}{\lambda_4}$$

or with the wavelength expressed in wave numbers

$$\frac{v_{overlap}}{c} = 1 - \frac{\sigma_3}{\sigma_4} = \frac{\Delta\sigma}{\sigma}$$

The present equipment may serve as a numerical example: distance between the laser mirrors is L = 44 cm $\Rightarrow$ $\Delta\sigma$ = 0.011363 cm^{-1} ; λ = 488 nm $\Rightarrow$ σ = 20491.76 cm^{-1} and finally

$$\Rightarrow v_{overlap} = 166 \text{ m/s}$$

For the case of the ideal geometry (i.e., source very close or behind the observer) described earlier, which results in an increase of the effect by a factor of 2, the actual velocity required for the overlap would be 1/2 · 166 m/s = 83 m/s.

The shift of the fringes was readily observed, as mentioned above. The maximum rotation rate of the homemade wheel was 50 rev/sec (at a setting of 500); with a radius of about 11 cm (where the laser light was incident), the maximum speed of the toothed wheel was about 35 m/s. The geometry was close to ideal with $\alpha \approx$ 135 degrees and $\beta \approx$ 22 degrees. Using the formula from page 3 this leads to

$$\Delta v/v \cong 1.71 \text{ v/c}$$

Obviously the present velocity was not fast enough to observe the actual overlap of the shifted and the stationary fringe rings. However the effect was very clear and especially dramatic when the system had been aligned so that either a constructive or destructive interference occurred at the center, because this resulted in the (dis)-appearance of the central disk. Brief videos of the fringes shifting with the velocity of the wheel were taped using a Loral CAM3000I image intensifier.

The following pictures are snapshots, taken at zero speed ("slow," "medium," and "maximum" speed of the wheel, Figure 7). The difference from Figure 6 is that the center of the pattern is found on the moving blade, thus causing the changing "bulls-eye."
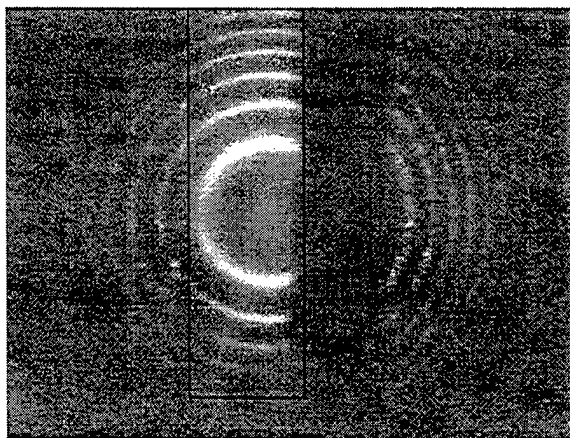
(a) Zero speed. Blade causes shadow to the right (laser illumination from left side).
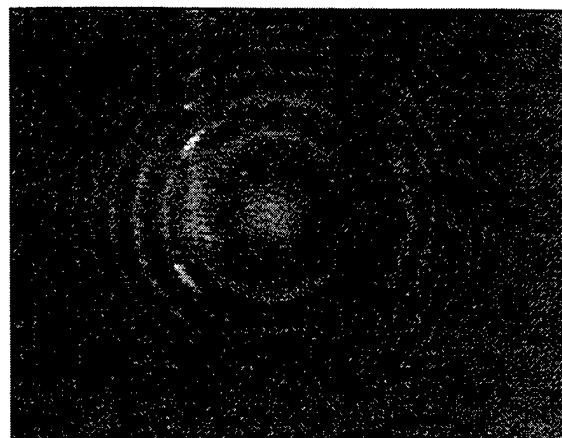
(c) Fast speed – new center appearing. Increasing discontinuity of outer rings.
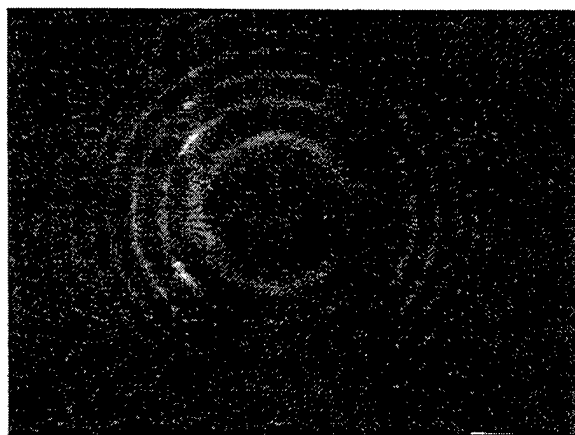
(b) Slow speed.
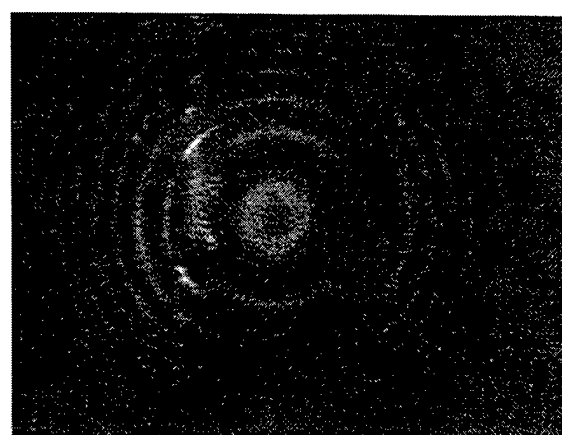
(d) Maximum speed (35 m/s) – center changing to ring.

FIGURE 7. Interference Patterns Observed in the Laboratory at Different Speeds.

Brief Summary for the Experimental, Active, Approach. For an active illumination/ diffuse reflection system capable of "resolving" small velocities (e.g., < 50 m/s = 180 km/h = 112 mph), one would want

- small mode spacing (i.e., long cavity, e.g., L = 1m, $\Delta\sigma$ = 0.005 cm^{-1})

- "blue" wavelength lasers (e.g., λ = 400 nm (σ= 25000 cm^{-1}))

which would bring overlap already at speeds of v $_{overlap}$ = 60 m/s.

To compare with the intensities available for the passive approach, one can estimate the intensity with which the present scene in the active setup is illuminated.

Power at the output coupler window of the laser is 45 mW. After reflection losses off a few mirrors, there remain about 25 mW for illumination of the scene with an area of approximately 1 cm^2. The photon flux at the scene is thus about $6 \cdot 10^{16}$ photons/cm^2/sec. Assuming a reflection coefficient of 1% and complete reflectance into a solid angle of 2π, one finds almost **10^{18} photons/(s m^2 sterad)** emitted from the scene.

Astronomers like to characterize their extended sources in R, which are defined by 1R = $10^{10}/(4\pi)$ photons/(s m^2 sterad). The conversion ratio is: **10^{18} photons/(s m^2 sterad)** corresponds to about **$1 \cdot 10^9$ R**. Another measure to describe the intensity of extended sources is in # photons/(s m^2 arcsec^2). The conversion ratio to R is **1kR = 18.7 photons/(s m^2 arcsec^2)**. Thus we have about **$20 \cdot 10^6$ photons/(s m^2 arcsec^2)** for detection purposes.

These numbers should be compared with the numbers given in the next section for the intensities of natural sources.

PASSIVE APPROACH

The passive approach is very similar to the active one except that nature itself will have to provide the illumination of the scene under observation. Sources that are only temporal in nature (such as auroras) will not be considered here because they are usually not available on the time scale of hours and they do not occur below certain geographical latitude. For now the focus will be on nighttime sources. Many of the daytime sources are the same as the nighttime sources but have the added complication that the background "noise" (sun light) is about 10^8 stronger.

An extensive literature search was performed to identify spectral lines occurring naturally in the sky that would be suitable candidates for the Doppler velocimetry project. Most of the experimental research characterizing the spectrum of the sky brightness was performed decades ago by astronomers who were annoyed by the presence of this ubiquitous light source in the background preventing them from obtaining measurements with a better signal to noise (S/N) ratio. Current research efforts in astronomy still deal with the identification and elimination of those lines, or with putting them to use as calibration sources for spectral investigations (Reference 5).

A general overview of the different type of light sources in the sky can be found in Reference 6. Depending on their origin these sources of the sky brightness are called (Reference 6):

- airglow (origin in the upper atmospheric levels)
- zodiacal light (scattered sunlight and thermal emission from interplanetary dust)
- integrated starlight (background only; individual stars can be accounted for separately)

- diffuse galactic light ("cirrus," mainly in the ultraviolet (UV) and visible spectra, reflected by interstellar dust; main source in the far infrared)

Keep in mind that the Doppler shift obtained would be a convolution of all the scattering angles (see first equation on page 4) because the source of the illuminating light is extended.

SOURCE INTENSITIES

The intensity of these sources and their overall spectral variation from 0.1 to 10,000 μm are reproduced from Figure 1 of Reference 6 as Figure 8 here. Doppler velocimetry via Fabry-Perot imaging desires narrow spectral lines (≈ 0.1 cm^{-1}) that are as intense as possible. It is obvious that airglow (OH and O_2) comprises the most intense source.
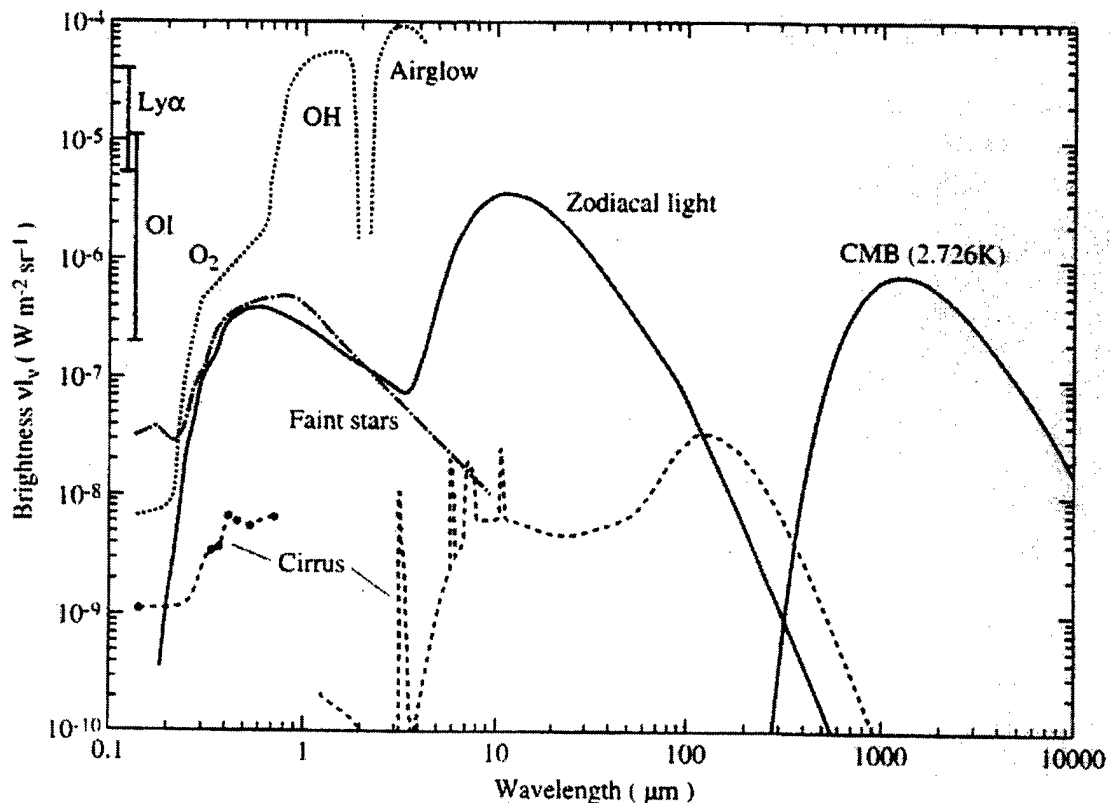
FIGURE 8. The General Brightness of the Night Sky Without Fine Details (From Reference 6).

The airglow itself has its origin in atmospheric layers surrounding the earth from about 100 to several hundred km above ground. This varies depending on the emitting molecule, e.g., for OH radiation the emitting layer is located from about 86 to 90 km above ground with a thickness on the order of 10 km, as illustrated by Figure 9.

This causes a rather interesting phenomenon called the "van Rhijn" effect: the observed amount of radiation increases with distance from the zenith because the length of the atmospheric column increases with angle (Reference 6). If an observer sets the zenith angle to $\alpha = 0$ degree and the location of the horizon at 90 degrees, then the radiation at 90 degrees is calculated to be about 7 times stronger.

With R being the earth's radius (6370 km) and h the height of the emitting layer above ground (90 km) (Reference 6), the van Rhijn increase in radiation from this layer with increasing angle from the zenith is given by:

$$van\ Rhijn(\alpha) = \frac{I(\alpha)}{I(\alpha = 0)} = \frac{1}{\sqrt{1 - z^2 \sin^2(\alpha)}}$$

with $z = R/(R + h)$.
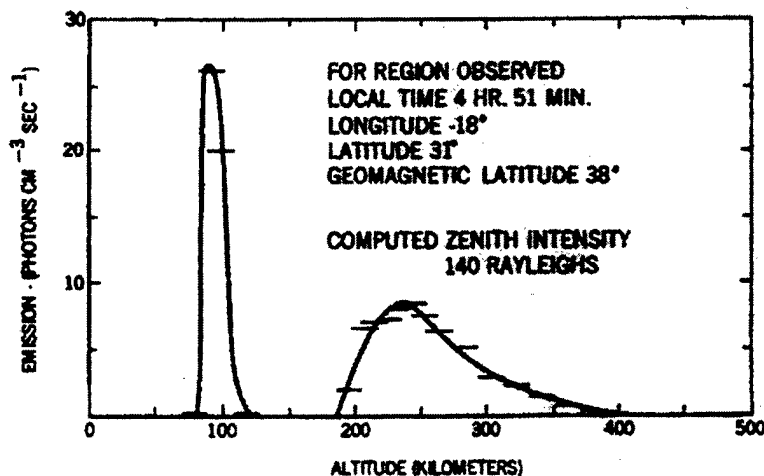
FIGURE 9. Height Profile of Airglow Emission as Measured by Satellite. The peak at 90 km originates with OH and the extended peak at higher altitude is due to OI emission (630 nm) (see Reference 7).

The van Rhijn factor is shown in Figure 10.

16
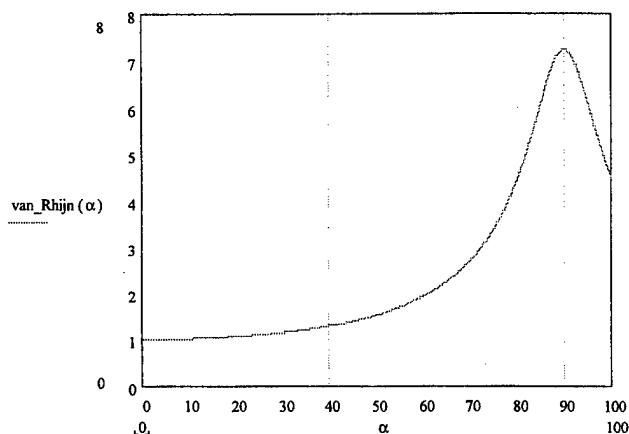
FIGURE 10. Increase in Radiation With Growing Angle From the Zenith ($\alpha = 0$): the van Rhijn Effect. Extinction and scattering are not included.

An atlas of sky brightness in the near-UV, visible, and near infrared (NIR) (310 to 1000 nm) is reproduced from Broadfoot and Kendall (Reference 8) and documented here as Figure 11. Measurements were taken at Arizona's Kitt Peak at an altitude of 2080 m (6824 ft) within 30 degrees from the zenith (i.e., no significant enhancement due to van Rhijn); the halfwidth (full width at half maximum (FWHM)) amounted to about 5 Å (instrument broadening). No corrections for the atmospheric extinction were made.

This measurement is somewhat typical for the observed intensities of the airglow. The intensity of the OI line at 5577 Å is near 200 R (Reference 8), a typical average value. However the OI lines at 6300 and 6364 Å were abnormally weak during the time of observation (References 6 and 8). This demonstrates the fluctuating intensities of the airglow that are by no means strictly constant with time and location, but are quite sensitive to changes either in the atmosphere itself or in the sun. Time scales can be on the order of minutes, and overall dependence also rests on the geomagnetic latitude showing a tropical enhancement (Reference 6). **The intensity of the radiation (spectral lines) as documented in Reference 8 increases from 1R/Å values in the UV at 310 nm gradually to more than 60 R/A at 1000 nm.**

This observation is also consistent with the difference in performance for night vision equipment. The response curve of generation III devices (GaAs-based) peaking at about 800 nm takes much better advantage of the stronger radiation in the NIR than generation II devices (whose spectral response is peaking at about 500 nm), which results in a big performance improvement for generation III over generation II.

As will be seen below, the number of photons available in the NIR between 1500 and 1800 nm is even larger than any numbers in the region around 800 nm and higher. Therefore any equipment operating between 1500 and 1800 nm should outperform

generation III sensors. This is based on the number of photons available in the different spectral regions.

A comment of clarification about published brightness values in Reference 9 must be stated. Reference 9 lists numerical values for individual lines and complete bands without showing any spectra. For example, a value of 1 kR is given for the nighttime O_2 line (from the atmospheric system b $\rightarrow$ X) at 864.5 nm. However, when looking at the following spectra, one finds that there is actually no narrow line at this wavelength, only the P and R branches of the band system, unsuitable for the present purpose (and their spectral brightness is less than 20 R/Å). Therefore the above value refers to the intensity of the complete band system; the use of the intensities listed in Reference 9 is not straightforward.
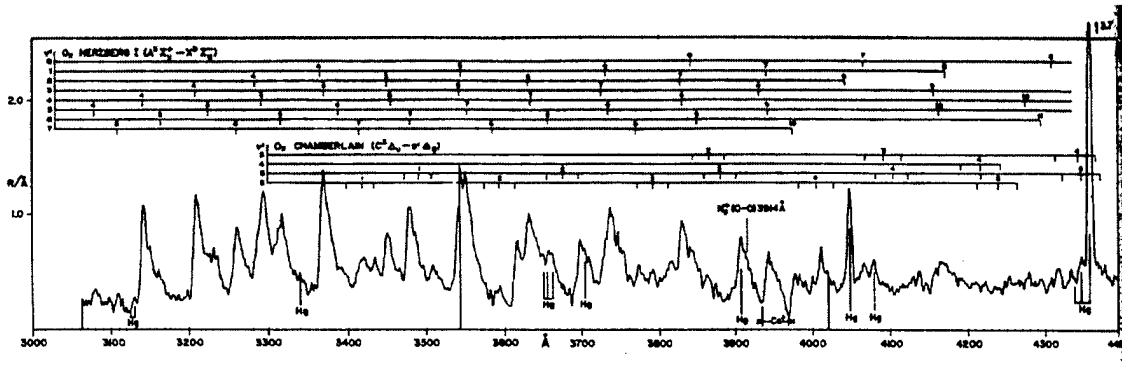
(a) 310 to 440 nm.
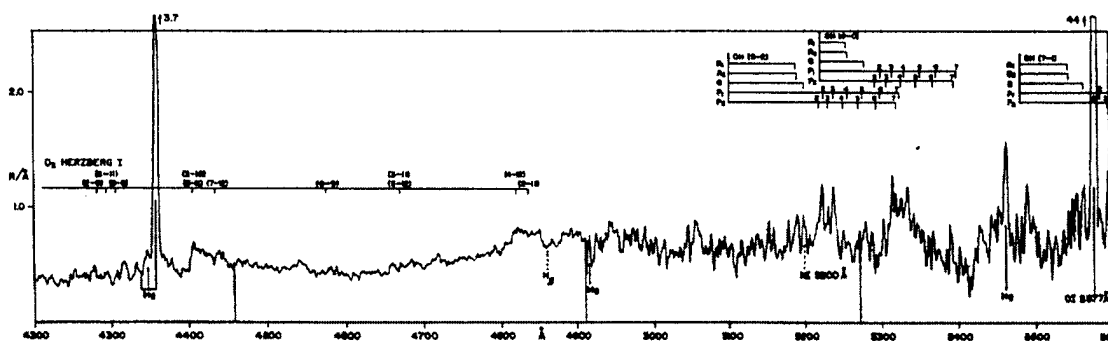
(b) 420 to 560 nm.

FIGURE 11. Atlas of the Sky Brightness at Night (From Reference 8).
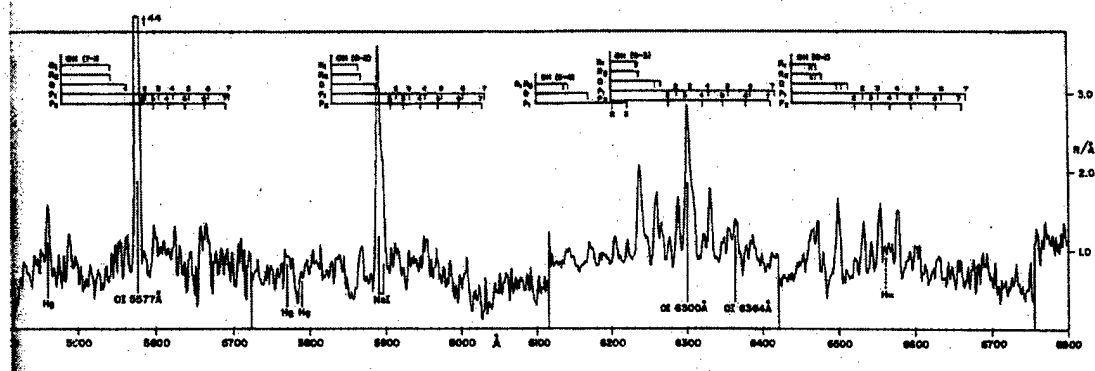
(c) 540 to 680 nm.
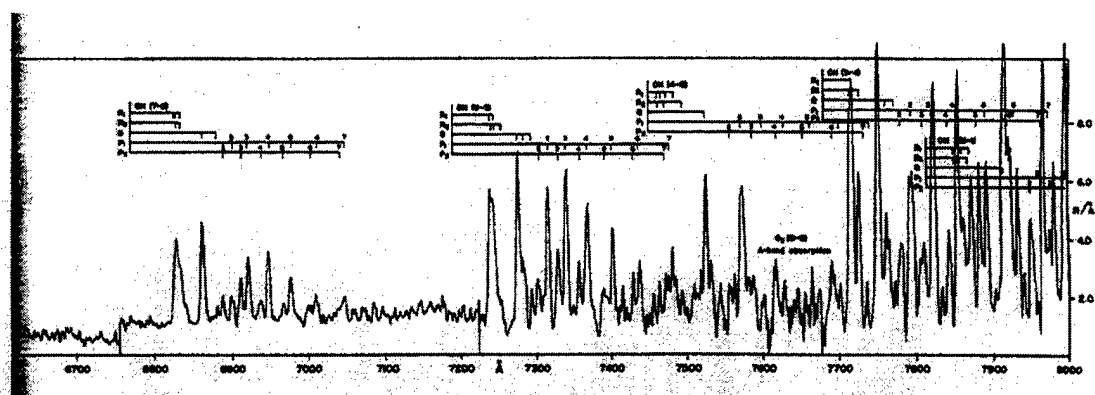
(d) 660 to 800 nm.
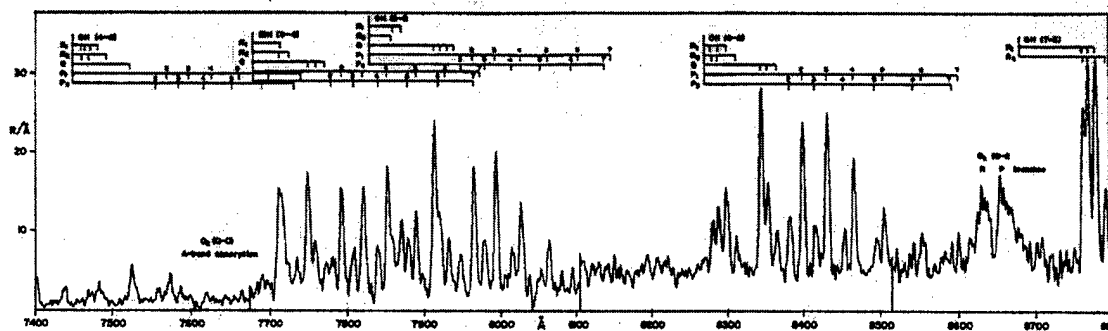
(e) 740 to 880 nm.

FIGURE 11. Contd.
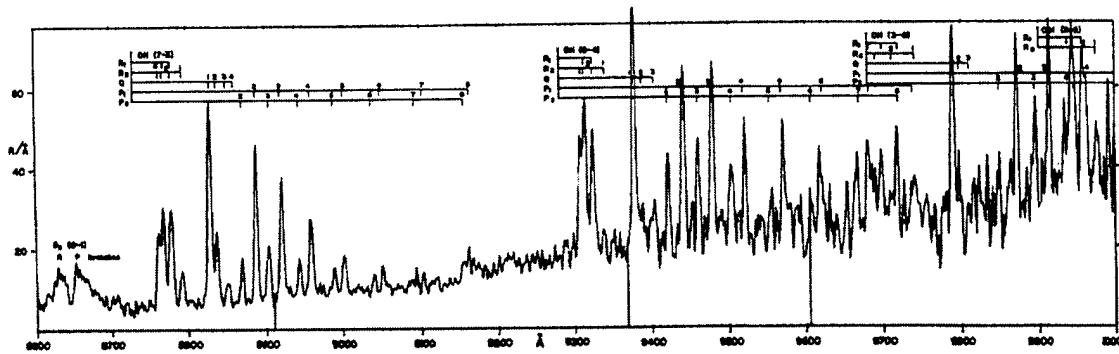
(f) 860 to 1000 nm.

FIGURE 11. Contd.

Investigations by researchers in the 1970s extended the spectral range of the nightglow. Steed and Baker used a "field widened" Fourier transform infrared (FTIR) to record the spectrum of the night sky from 900 to 2300 nm in a ground-based observation of the zenith midnight sky at White Sands, New Mexico, reproduced here as Figure 12 (Reference 10). Whereas Broadfoot and Kendall gave their results in R/Å, Steed and Baker gave theirs in $kR/cm^{-1} = kRcm$ with cm^{-1} as the unit for the inverse wavelength $1/\lambda$. The numerical values are equal for 1000 nm; however at 1.65 µm, the result given in R/A is 2.72 smaller than the result given in Rcm. In general, the OH lines between 1.50 and 1.80 µm are the strongest lines of the nightglow accessible to a ground-based observer (more than a factor 20 stronger than the ones up to 1000 nm).

Maihara, and others (Reference 5) made more recent observations (in 1993) of the OH airglow from Mauna Kea with the 2.2-m telescope (4214 m or 13824 ft. above sea level). They gave detailed band positions and intensities. The 10 strongest lines, all of them OH, are reproduced in Table 3. Page 14 of this report lists the conversion between R and (photons s^{-1} m^{-2} $arcsec^{-2}$).

TABLE 3. The 10 Strongest Lines in the NIR (After Reference 5). γ = photon; *: recalculated from Reference 10.

Number (from Reference 5)	Wavelength λ (μm) (in vacuum)	Intensity (γ s^{-1} m^{-2} arcsec^{-2})	λ (from Reference 5) (μm) (in vacuum)	Intensity (from Reference 10) (kR/cm^{-1}) (kR/A)*	
20	1.58334	338	1.58332	2.30	.917
24	1.60312	299	1.60308	1.53	.595
26	1.61290	296	1.61286	1.71	.657
28	1.62351	297	1.62354	1.27	.481
42	1.66925	431	1.66921	2.30	.825
46	1.69034	244	1.69037	1.45	.507
48	1.70083	301	1.70088	1.80	.622
64	1.76531	363	1.76532	2.00	.642
68	1.78808	268	1.78803	1.20	.375
69	1.79942	204	1.79940	1.42	.439

Note: It is quite likely that Maihara (Reference 5) measured the intensities within 20 degrees to the horizon, so that the van Rhijn effect would have caused their intensities to be enhanced by a factor of 2.7 (see Figure 9).

The measurements of Reference 10 had a resolution of 2-3 cm^{-1} that brings the spectrally integrated intensity of the strongest line (42 in the table above) to ca. 6.9 kR (compared to the OI intensity at 5577 Å that runs at about 0.2 kR at night). Reference 5 measures 431 γ s^{-1} m^{-2} arcsec^{-2} for this line, which would correspond to 23 kR; taking the van Rhijn enhancement into account, this reduces to 8.5 kR, a comparable value to the 6.9 kR considering the different locations and dates of the observations as well as the patchy and temporally varying behavior of the airglow.
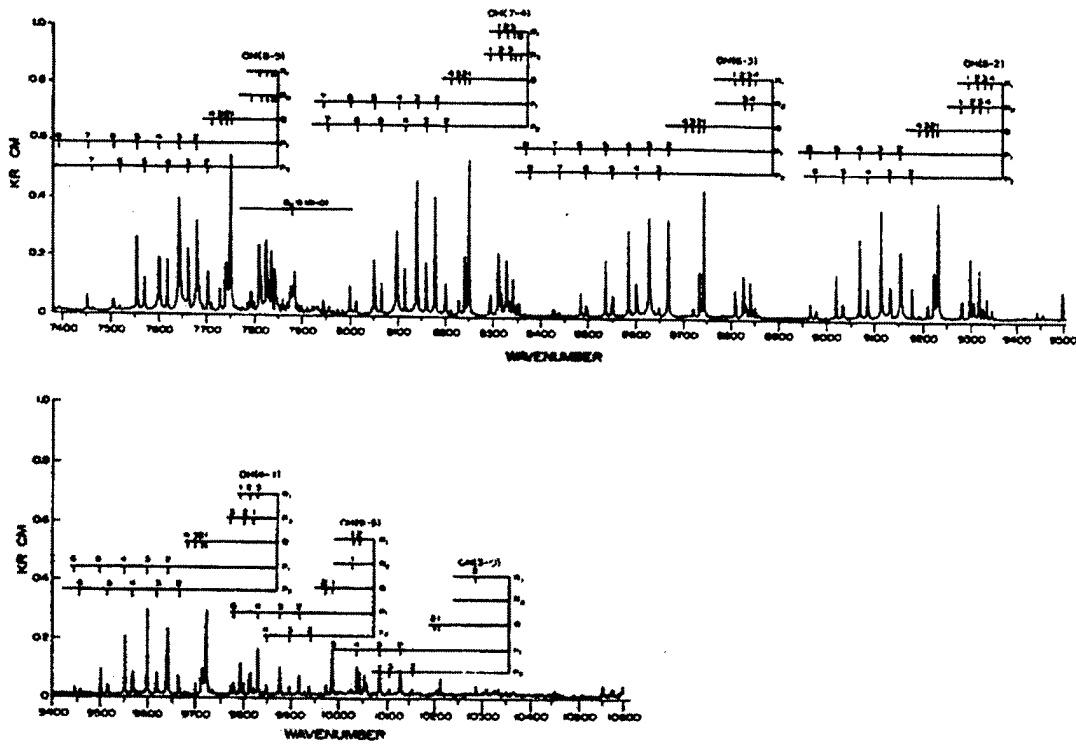
Fig. 2. Continuation of Fig. 1.

(a) 7400 to 10500 cm^{-1} or 952 to 1351 nm.

FIGURE 12. Intensity of the Airglow (Mainly the OH Meinel Bands) From Reference 10.
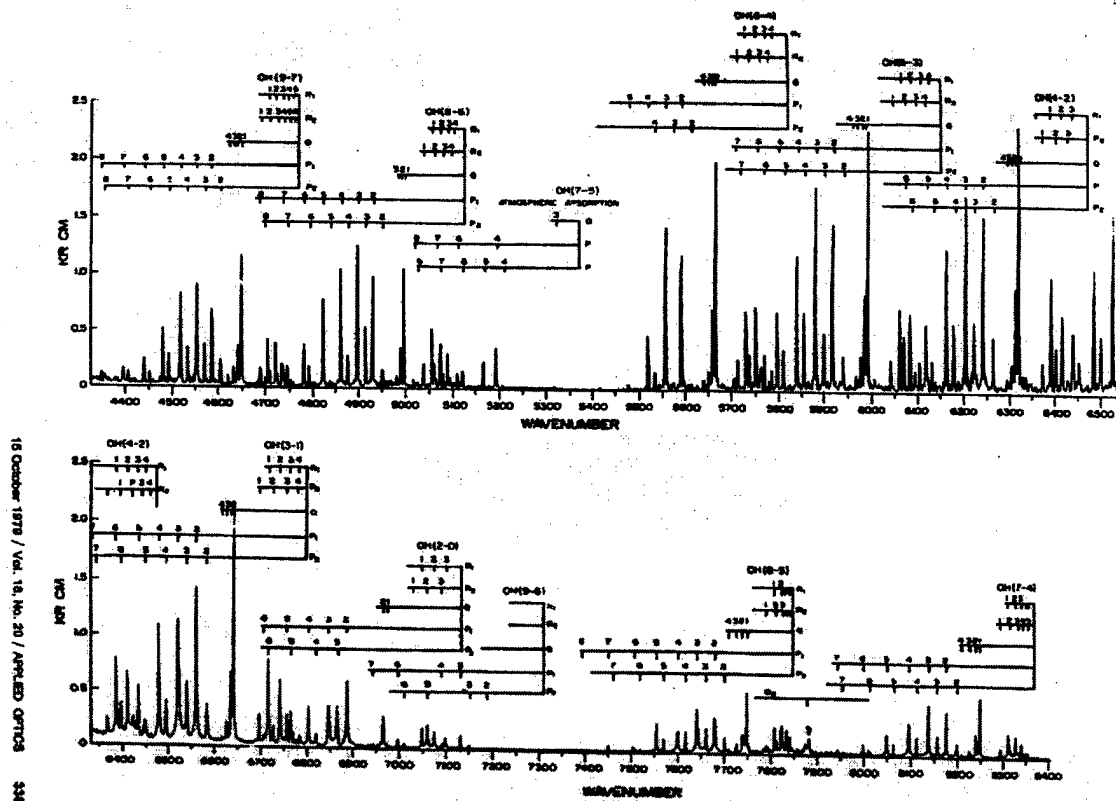
Fig. 1. Night sky emission spectrum taken at White Sands, New Mexico, December 1975.

(b) 4400 to 8400 cm⁻¹ or 1190 to 2273 nm.

FIGURE 12. (Contd.)

According to this small review of airglow (nighttime) measurements, the OH Meinel line at 1.66925 μm (from the OH 5-3 vibrational transition - $\Delta v = 2$) is the strongest line available. The Doppler-shifts one can expect at this wavelength (1660 nm) are listed in Table 4. The Doppler-width is assumed to be 0.043 Å or 469 MHz (see page 26).

TABLE 4. Doppler Shifts at a Wavelength of 1660 nm Based on $\Delta v/v \cong v/c$. The formula $\Delta v/v \cong v/c$ is used; therefore the effect could be twice as much in the ideal case.

Velocity (m/s)	(mph)	(km/h)	Doppler shift (MHz) λ=1660 nm [$1.81 \cdot 10^{14}$ Hz]	Doppler shift (A) λ=1660 nm	Doppler-broadening/ Doppl. shift
10	22.5	36	6.0	0.00055	78.2
20	44.4	72	12.1	0.00111	38.7
30	67.5	108	18.1	0.00166	25.9
50	112.5	180	30.2	0.00277	15.5
80	180	288	48.3	0.00443	9.7
100	225	360	60.3	0.00553	7.8
300	675	1080	181	0.01660	2.6
500	1125	1800	302	0.02767	1.55

Following the strong OH radiation up to 2.3 μm, there is a radiation "hole" at 2.4 μm that is simply the gap between the $\Delta v = 1$ and $\Delta v = 2$ progression of the OH radical. Strong atmospheric absorption due to water and CO_2 follows between 2.5 to 3.5 μm. Spectral features beyond 2.3-μm wavelength are inaccessible to ground observation but have been measured using balloons as experimental platforms (References 11 and 12). Figure 13 is an example of their intensity as measured by a ground observer (albeit on a mountaintop). This measurement was performed on Mauna Kea 13800 ft above sea level ($\approx$ 4200 m) (Reference 13). From this height there can be seen a small hint of these at sea level—inaccessible bands whose spectra are much more intense at heights greater than 25 km (References 11 and 12).
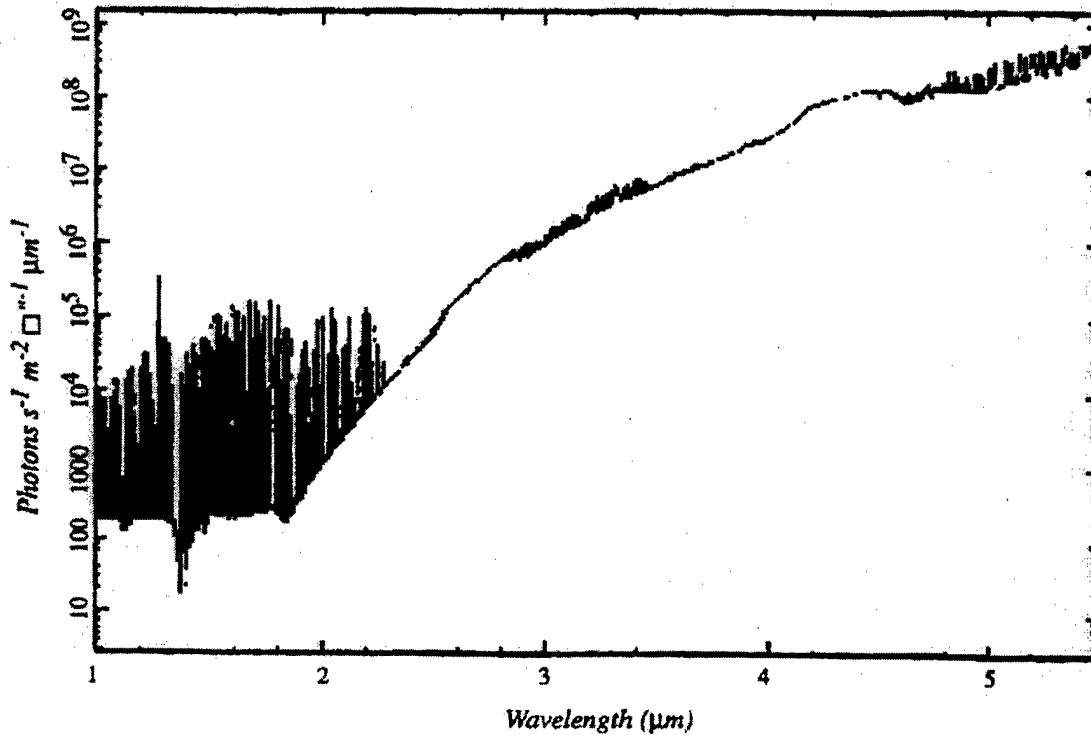
FIGURE 13. Intensity of the Nightglow Observed Just Inside the Cryostat Window of the UKIRT IRCAM Camera (Mauna Kea, Altitude About 4200 m) (Reference 13).

LINEWIDTH

As outlined above, for Fabry-Perot Doppler velocimetry of fast moving objects, spectrally narrow lines are wanted. Most of the lines of the airglow (especially the OH Meinel lines) are of atmospheric origin at high altitude and therefore only Doppler broadened (pressure broadening can be neglected at the densities under consideration (Reference 5)). In fact, for altitudes higher than 75 km in the atmosphere, Doppler broadening is the main broadening mechanism, more important than pressure or collisional broadening. It has been observed that most of the line temperatures are on the order of 200 to 250 K (Reference 14), which gives Doppler broadening values of less than 0.1 cm^{-1} at a wavelength of 1.65 μm. In general, the formula for Doppler broadening is

$$\Delta v(FWHM) = 2\frac{v}{c} \cdot \sqrt{2ln2} \cdot \sqrt{kT/M}$$

with $(2kT/M)^{1/2}$ the most probable velocity (see Reference 15). Instead of the frequency v, one can substitute the wave number σ or the wavelength λ and obtain the FWHM in

25

those units. With the temperature T in K and the molecular mass M in amu the formula can be rewritten as

$$\Delta\sigma(FWHM) = \sigma \cdot 7.14 \cdot 10^{-7} \sqrt{T/M}$$

Again, instead of the wave number σ one could just as well use wavelength or frequency units.

Figure 14 shows the temperature distribution in the atmosphere (taken from Reference 16). It appears that the layer close to an altitude of 90 km has the coldest temperature and therefore the emission originating from that altitude—the OH Meinel radiation—has the smallest linewidth. Other types of radiation, e.g., the radiation generated by the OI atoms between 200 to 350 km altitude, exhibit a much larger linewidth because the temperature is much "hotter" (around 1000 K for the OI emission). Therefore, radiation emitted by OI is not only less intense than the OH Meinel bands but also spectrally wider, thus potentially compromising the sensitivity of a Doppler measurement.

As an example, for 220 K and OH as the molecule, one obtains at $\lambda = 1.66 \ \mu m$ (6024.1 cm^{-1} or $1.807 \cdot 10^{14}$ Hz) a Doppler FWHM of 0.043 Å (0.0155 cm^{-1}, 0.464 GHz).

A comparison of the Doppler *width* of the OH Meinel line with the Doppler *shift* of the line due to velocity is shown in the last column of Table 4. It is possible that the temperatures and thus the linewidths are even lower. Reference 17 finds "rotational" temperatures of 163 K on a particular date, corresponding to values of 0.037 Å (0.0133 cm^{-1}, 0.400 GHz). The temperature shows a cyclical behavior on the order of hours each night, e.g., it can vary between 180 and 195 K (Reference 18).
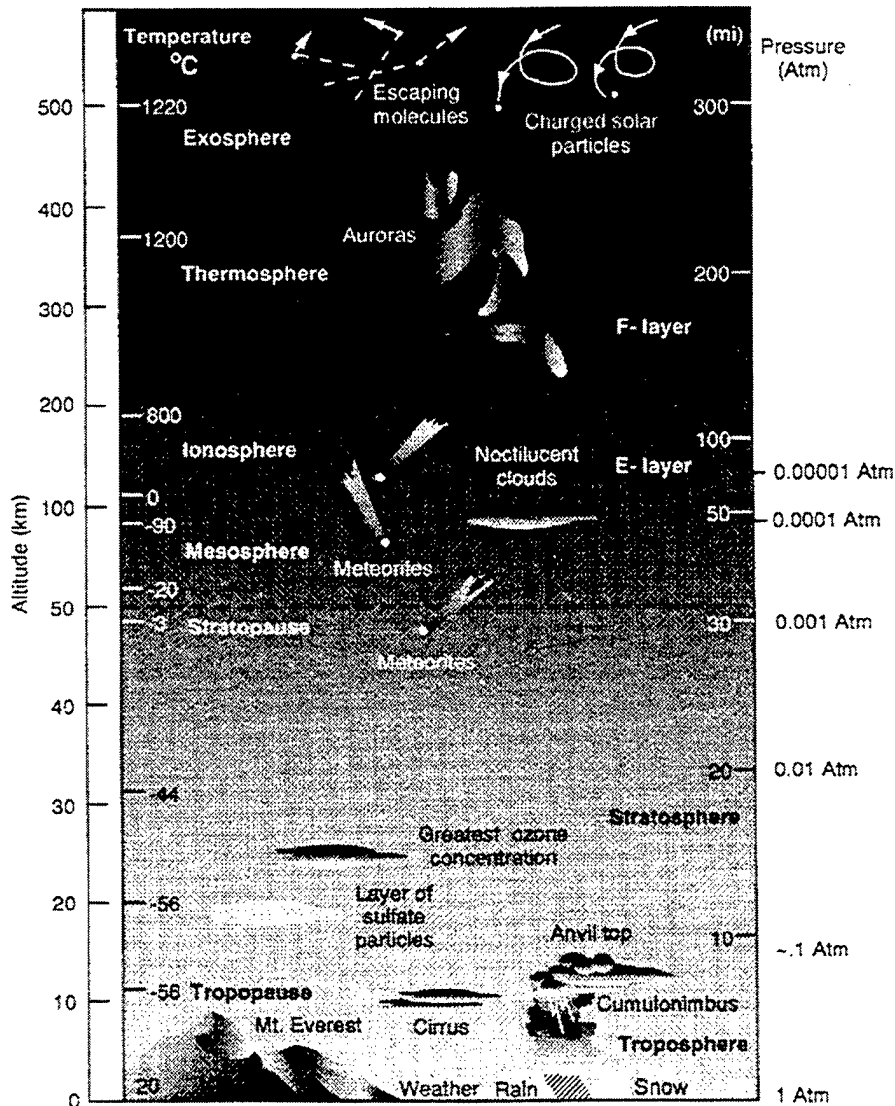
FIGURE 14. Earth's Atmospheric Layers With Their Temperatures and Pressures (From Reference 16, Page 8).

THE OH MEINEL BANDS

Based on all the arguments above, the emission of the OH molecule in the NIR constitutes the best source for natural illumination with respect to intensity and line-width. The emission is generated in a few-km-thickness layer of the atmosphere at an altitude of about 87 to 90 km. Detailed information about this fairly, unique molecule has been collected over the years. One of the features pertinent to the present objective is that the emitted radiation, the OH Meinel bands, actually consists of fine structure doublets. The figure axis of the molecule has a small but non-vanishing moment of inertia, which leads to the so-called "Λ-doubling" (i.e., every OH rotational state consists of a pair of closely spaced levels: Reference 19). Additionally, the ground state forms a doublet ($^2\Pi_{1/2}$ and $^2\Pi_{3/2}$) and therefore the OH Meinel bands consist of two subbands of

which the one belonging to the $^2\Pi_{3/2}$ system is by far the stronger. The strongest lines of these are the Q_1 (1) doublets – the spectral distance between the members of the doublets is variable and increases with the rotational quantum number J.

Abrams and others have performed high resolution FTIR spectroscopy of the Meinel system of OH (Reference 20). In their experiment they tried to imitate the conditions in the upper atmosphere and used a gas pressure of 4 Torr and T ≤ 300 K while reacting gaseous ozone and dissociated hydrogen. Table 5 lists the band positions they found for the rotationally lowest Q_1 branches of the $\Delta v = 2$ sequence, which are the most intense lines in the airglow (but not in their experiment because the states were populated by a different mechanism). Q_{1e} and Q_{1f} denote the Λ-doubled lines. Q_{1e} should be identified with the $^2\Pi_{3/2}$ system.

TABLE 5. Spectral Positions of Some of the Strongest OH Meinel Lines Observable. 10 → 8 only observed by Abrams (Reference 20).

Vibrational transition	Q_{1e} branch ($^2\Pi_{3/2}$)	Q_{1f} branch ($^2\Pi_{1/2}$)
2 → 0	6971.2909 cm^{-1} 1.4344545 μm	6971.3936 cm^{-1} 1.4344334 μm
3 → 1	6642.0228 cm^{-1} 1.5055654 μm	6642.1173 cm^{-1} 1.5055440 μm
4 → 2	6315.7718 cm^{-1} 1.5833378 μm	6315.8585 cm^{-1} 1.5833160 μm
5 → 3	5990.7183 cm^{-1} 1.6692489 μm	5990.7972 cm^{-1} 1.6692269 μm
6 → 4	5664.6534 cm^{-1} 1.7653331 μm	5664.7243 cm^{-1} 1.7653110 μm
7 → 5	5334.8569 cm^{-1} 1.8744645 μm	5334.9201 cm^{-1} 1.8744423 μm
8 → 6	4997.9297 cm^{-1} 2.0008285 μm	4997.9864 cm^{-1} 2.0008058 μm
9 → 7	4649.5613 cm^{-1} 2.1507405 μm	4649.6120 cm^{-1} 2.1507171 μm
10 → 8	4277.2337 cm^{-1} 2.3379597 μm	4277.3907 cm^{-1} 2.3378739 μm

The theoretical intensity distribution of almost all the OH Meinel (rotational P-branch) vibrational sequences has been estimated by Chamberlain and the relevant plot from Reference 15 is reproduced here as Figure 15.
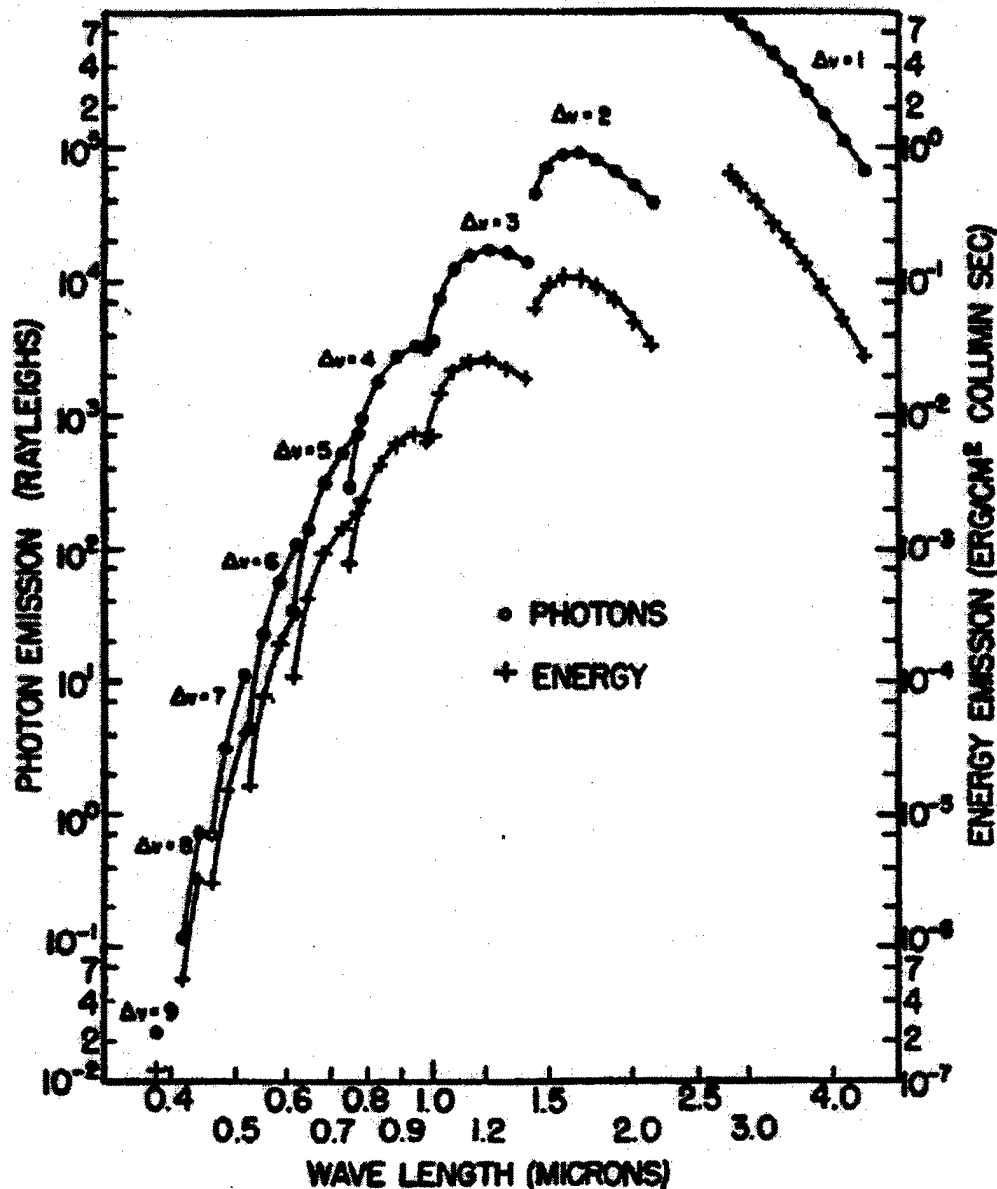
FIGURE 15. Predicted Photon Emission Rates in Rayleighs and Energy Emission Rates in erg/cm^2 (Column) sec for the OH Meinel Bands. For each vibrational sequence (v' → v") the starting point v' = 9 is on the right (from Reference 15, page 555).

Note that almost all the bands of the Δv = 1 sequence are estimated to have higher emission rates than those of the Δv = 2 sequence. However as pointed out before, they are inaccessible to ground based observation (References 12 and 13). The 1 → 0, 2 → 1, 3 → 2, 4 → 3 and 5 → 4 transitions are heavily impacted by atmospheric constituents, mostly water and CO_2. Also, Figure 13 shows the intensity distribution over a larger spectral range, measuring that the Δv = 2 sequence is received much more strongly. Bands of this sequence that are heavily impacted by atmospheric absorption (H_2O) are the

$2 \to 0$ and the $7 \to 5$. Bands $8 \to 6$, $9 \to 7$, and $10 \to 8$ are all progressively weaker. Thus the most promising candidates are the Q_1 (1) bands of the vibrational transitions $3 \to 1$, $4 \to 2$, $5 \to 3$, and $6 \to 4$.

RADIATION PROPAGATING THROUGH THE ATMOSPHERE

The following section will calculate the total light flux incident on the surface S of the target (located at the origin of the angle α) in order to obtain a numerical estimate of the light flux reaching the observer. For simplicity S is held up vertically, thus oriented along a radial line from the earth's center. The incident radiation originates within the ionospheric E-layer at about 90 km (Reference 6). Figure 16 depicts the situation schematically: α is the angle of an observer at the target with the zenith and θ is the polar angle to the center of the earth from spherical coordinates. The parallel circular lines depict the light-emitting layer that is at a height h above ground, and d is the distance of the observer to this layer in the direction of observation. R is the earth's radius (6370 km).

FIGURE 16. Geometry of the Earth's Atmospheric Layers.

First natural phenomena and effects could prevent the OH radiation from reaching the ground. The OH Meinel bands between 1 to 2 μm will be of particular interest, especially the strongest lines close to 1.6 μm. Geometrical references below are will be based on Figure 16.

Influence of Molecular Scattering

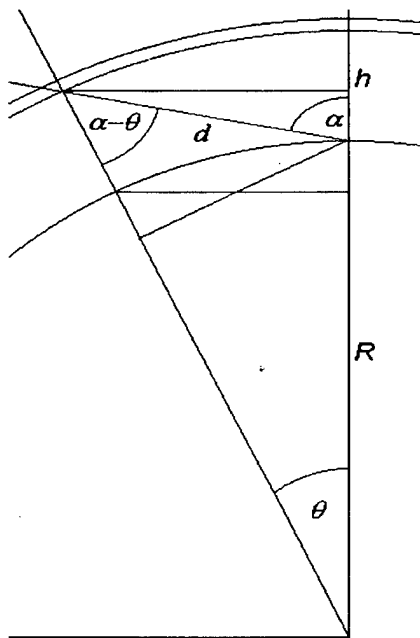The influence of molecular scattering, be it nitrogen or oxygen molecules, is negligible. The formula below gives the scattering coefficient per unit volume (unit: 1/m) (Reference 16). In other words the reciprocal of the value gives the scattering length after which 1/e of the wavelength experiences scattering. The IR/EO Systems Handbook (Reference 16) gives the scattering coefficient as

$$\sigma_{SCA}(h) = \frac{8\pi^3 \left(n^2 - 1\right)^2 N(h)(6+3\delta)}{3N^2(0)\cdot\lambda^4 \qquad (6-7\delta)}$$

with N (h) the number density at a height h, λ the wavelength, n the index of refraction of air, and δ the depolarization factor from the anisotropy of the gas molecules. According to Reference 16, the accepted value is $\delta = 0.035$. If one sets h = 0, then typical values in the visible are in the range of several tens of km for blue light, about 4 times as much for red light, and several thousand km for a wavelength of 1.66 μm. Molecular Rayleigh scattering will therefore not measurably contribute to a decrease in the photon flux.

Influence of Aerosol Scattering and Atmospheric Absorption

Aerosol scattering is more tedious to assess than molecular scattering. There are numerous models for size distributions of particles, their index of refraction, and extinction coefficient (Reference 16). A detailed assessment is beyond the scope of this report. However, the following observations might help to get a feel for the order of magnitude of the effect. The path of the light from the light emitting layer to the surface S of the target has a length of d km, given in Table 6.

TABLE 6. Distance d From Light Emitting Layer to Target S for Different Angles α and Length Traveled in the Troposphere. The last column refers to the path within the lowest aerosol layer where the content is determined by meteorological conditions.

Angle α with zenith (degrees)	Distance d (km)	Path traveled within $h \le 10$ km layer: troposphere	Path traveled within $h \le 2$ km layer
90	1075	357	160
85	654	105	22.5
80	436	56	11.5
75	319	38	7.7

Usually, natural obstacles (trees, hills) or man-made objects prevent radiation emitted under an angle α between 80 and 90 degrees from reaching a ground based observer. The OH radiation will probably not have to travel more than 10 km in the lowest ($\leq$ 2-km altitude) layer of the atmosphere (and that only for large α).

Around 20 km above ground there is a layer of sulfate particles, with the actual troposphere extending from the ground to slightly higher than 10 km. Reference 16, page 103, shows the layer scheme for different aerosols, depending on the height above ground; Table 6 shows that a significant fraction is spent in the last 10 km and especially in the lowest 2 km. Depending on the conditions (snowfall, sandstorm), this could potentially prevent any light with a wavelength of 1.66 μm from reaching the target. However, the measurements in References 5 and 10 were made from the ground at night, one on top of Mauna Kea, Hawaii, and one at the White Sands Missile Range, New Mexico. Even though no atmospheric conditions were listed for the time of measurement, it is felt that the atmospheric transmission for this type of radiation is quite good for the following reasons: When using the LOWTRAN method as outlined in the Reference 21, together with standard models for the atmosphere, one can estimate the effect of aerosol scattering on the transmission rather quickly. This results in Figures 5 through 14 on pages 5 through 59 of Reference 21, which gives the transmission for a path of 1 km together with scaling factors for longer pathlengths. For 1 km the transmission is higher than 90%, for 5 km it is still above 70%, and for 10 km it is above 50%.

In general, atmospheric transmission is in general better in the IR than in the visible. How the atmospheric absorption qualitatively affects the airglow at night between 1.3 and 1.9 μm can be immediately gathered from Figure 17 (taken from Reference 14). The strong OH Meinel spectral lines are found in a window in between major atmospheric absorption due to water bands and thus should also be accessible at times of high humidity and cloud cover.
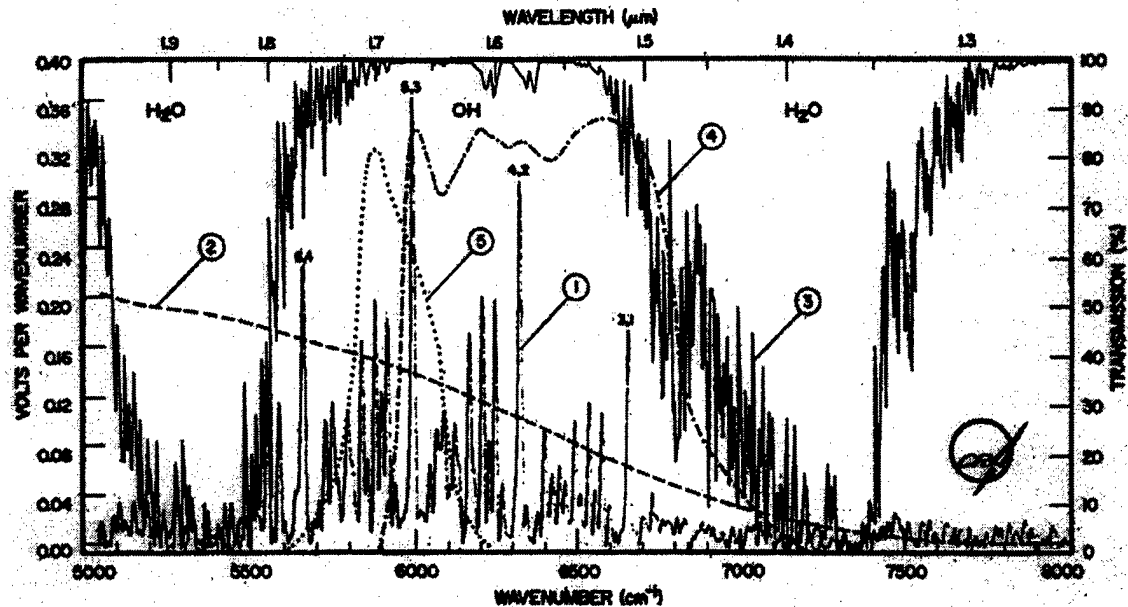
FIGURE 17. Influence of the Atmospheric Absorption on the Sky Brightness in the NIR (From Reference 14). 1: intensity; 2: instrument response; 3: theoretical atmospheric transmission; 4, 5: filter curves.

Gebbie and others (Reference 22) find a transmission of almost 80% for 1.66 μm in a wavelength window reaching from about 1.5 to 1.8 μm for a pathlength—mainly above ocean at a height of 100 feet above sea level—of 1.829 km (2000 yd). The environmental conditions were 17-mm water content (the height of the water level precipitated out of the atmosphere for a column of a particular length) at a visual transmission of 60% at 0.61 μm.

Taylor and Yates (Reference 23) measured the transmission from 0.5 to 15 μm over a pathlength of 5.5 (curve B) and 16.25 km (curve C)—3.4 and 10.1 statutory miles. The maximum transmission in the 1.5- to 1.8-μm window is at about 65 and 45%, respectively (conditions are 47 and 48% relative humidity at 34.5 and 40.5°F, precipitable water of 13.7 and 52.0 mm with visual ranges—defined as daylight meteorological range—of 16 and 24 miles, respectively). The relevant figure of their publication is reprinted as Figure 18. The optical paths corresponding to curves A, B, and C led over land (A) and ocean water (B and C). For path C the light traveled across the Chesapeake Bay.
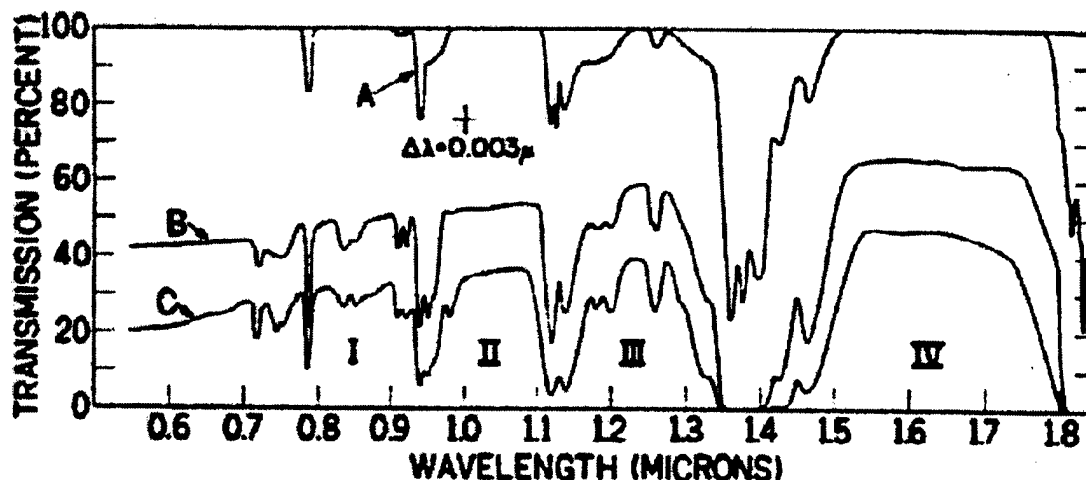
FIGURE 18. Transmission Curves Measured on 20 and 21 March 1956 by Taylor and Yates (Reference 23). Curve A: 300 m (37°F; 62% humidity; 22 miles visual range); curve B: 5.5 km (34.5°F; 47% humidity; 16 miles visual range); curve C: 16.25 km (40.5°F; 48% humidity; 24 miles visual range).

Streete's measurements stretched over a horizontal path of 25 km near Cape Kennedy (21 m above sea level) (Reference 24). He states that ". . . the window region around 1.67 μm is almost entirely free of absorption bands, so the extinction coefficient at this wavelength should be accurate." For precipitable water vapor of 215 to 254 mm he finds maximum transmission values of close to 8% in the 1.5- to 1.8-μm spectral region. At 362 mm he still finds more than 6% that drops to ca. 3% for 433-mm water content.

Espy and Hammond calculated the atmospheric transmission for some of the OH Meinel bands in the NIR using the FASCOD2 program (effects of aerosol were not included) (Reference 17). The optical path was from the zenith straight down. For the strongest Q1 (1) lines of the 3-1 and 4-2 vibrational transitions, they find the following transmission coefficients (Table 7):

TABLE 7. Atmospheric Transmission Coefficients for a Vertical Path From Zenith to Ground (From Reference 17).

Band	Mid-latitude summer	High-Latitude summer	Mid-latitude winter	High-latitude winter
3-1 OH; 1.5056 μm	0.922	0.947	0.979	0.991
4-2 OH; 1.5833 μm	0.957	0.968	0.986	0.992

In summarizing the influence of atmospheric absorption, one finds in general that the 1.5- to 1.8-μm spectral regions does not offer as high a transmission as the 3.5- to 4.0-μm

or the 9- to 12-μm region but both of these do not contain strong narrow natural spectral lines. On the other hand, some of the strongest OH Meinel lines are located within the 1.5- to 1.8-μm window, which offers superior transmission with regard to wavelengths in the visible.

It is felt that for reasons of intensity (strongest lines), linewidth (smallest Doppler broadening), and spectral position in an atmospheric transmission window, the OH Meinel bands between 1.5 and 1.8 μm constitute the best natural source available for the project.

Radiation Incident on a Target With Diffuse Reflection Only

The following calculation is based on this simple model: spherical earth surrounded by a thin radiation emitting layer at h = 90 km above ground. The target is held vertical on the earth's surface with a polar angle θ = 0.

This is the first extreme case to be addressed. Because the target is diffusely reflecting only, one has to calculate the incident flux received from the whole spherical layer capable of having a line of sight to the (front) surface of the target. The emitting layer is split up in parallel slices defined by the angle α with the zenith. One has to incorporate all the contributions of the azimuthal angles φ (from 0 to π) with φ = π/2 defining the direction normal to the surface (when α = π/2), and then integrate over all the slices. From the schematics in Figure 16 (also see Reference 15) one can find that

$$d \cdot \sin(\alpha - \theta) / d \cdot \sin(\alpha) = R / R + h = z$$

The layer thickness at an angle α will then be increased by the van Rhijn factor of

$$\frac{1}{\cos(\alpha - \theta)} = \frac{1}{\sqrt{1 - z^2 \sin^2(\alpha)}}$$

With φ the azimuthal angle, the surface element of the light emitting layer is

$$dA = d\varphi \cdot d\theta \sin\theta \cdot (R + h)^2$$

The distance of an area S(vertical) located at the observer to the area element dA can be obtained from

$$d^2 = R^2 + (R + h)^2 - 2R(R + h)\cos\theta$$

35

The solid angle $d\Omega$ of the radiation leaving a layer element dA and striking S is given by

$$d\Omega = S \cdot \sin\alpha \cdot \sin\varphi / d^2$$

The total incident radiation can be found by integrating over φ from 0 to π and the angle α from 0 to $\pi/2$ or somewhat more, namely $\alpha_T = \pi/2 + \arccos[R/(R + a)]$ if the surface S is not at ground but at a height a above.

With "$J \cdot t_0$" being the sky brightness in photons/(s m^2 sterad), taking the van Rhijn effect of a layer with thickness t into account the integration to be performed is

$$N\left(\#\gamma / \left(sm^2\right)\right) = Jt_0 \int_0^\pi d\varphi \sin\varphi \int_0^{\theta_T} d\theta \sin\theta \cdot \frac{\sin\alpha}{\sqrt{1 - z^2 \sin^2\alpha}} \cdot \frac{1}{1 + z^2 - 2z\cos\theta}$$

with ($\cos\theta_T = \dfrac{R}{R + h}$), which can be further transformed using

$$\sin\alpha = \frac{\sin\theta}{\sqrt{1 + z^2 - 2z\cos\theta}}$$

Evaluating the integral with a commercially available application like Mathcad™, one obtains numerical results depending on the maximum angle α. It is ideally $\pi/2$ for a ground-based observer, but landscape, houses, trees, and other obstacles can limit the range dramatically. Table 8 lists the results in terms of a numerical factor times the source strength "Jt_0," meaning that "$J \cdot t_0$" has to be multiplied by this numerical factor, which then gives the number of photons striking the surface S.

TABLE 8. Intensity Factor and Photon Flux for Different Zenith Angles.

Maximum angle α with zenith	Maximum polar angle θ with zenith	Intensity factor	Total number of photons (γ) onto surface S of 1 m^2 in 10^{12} γ/sec
90	9.575	16.19	89
89	8.627	14.94	82
88	7.780	13.11	72
87	7.030	12.53	69
86	6.370	11.41	63
85	5.791	10.38	57
84	5.285	9.44	52
83	4.842	8.58	47
82	4.453	7.80	43
81	4.112	7.11	39
80	3.811	6.48	36
79	3.545	5.92	33
78	3.308	5.41	30
77	3.097	4.96	27
76	2.907	4.55	25
75	2.736	4.18	23

The calculation does not incorporate lower atmospheric scattering due to aerosols and other light scattering absorbing phenomena. The case of molecular scattering was already found to be negligible.

These numbers are meant more as estimates when looking at the simplicity of the model. They also demonstrate one more time the importance of the van Rhijn effect, which increases the intensity factor for angles α close to the horizon. If S = 1 m^2 and Jt_0 = 6.9 kR (spectral line 42 from Table 3 multiplied with 3-cm^{-1} resolution)—which is very optimistic since the individual lines of the fine structure must be less—then the total number of incident photons per second onto the area S is $\approx$ 16·6.9 kR sterad m^2 or 8.8 10^{13} photons/s for $\alpha = \pi/2$. More realistic angles of 80 and 75 degrees result in reduced photon numbers of 3.6 and 2.3·10^{13} photons/s.

Target S of 1 x 1 m at 10-km Distance From Observer

After estimating the total incident flux on the target, one has now to find the radiation scattered toward an observer. If one moves the observer r = 10 km away from the surface S of the target, the solid angle of the ideally diffusely reflecting (100%) surface S with respect to the observer is 20.6 x 20.6 arcsec. The intensity emitted per area at this distance is (assuming a number of photons of about $3 \cdot 10^{13}$ photons/s is incident on the target, i.e., $\alpha = 78$ degrees)

$$3 \cdot 10^{13} / \left(2\pi r^2 \right) \approx 48000 \text{ photons/m}^2$$

Assuming an aperture of the detector/receiving optics of 1 foot diameter = 0.073 m^2 a total of $\approx$ **3500 photons/sec** is received by the observer.

A FPA (focal plane array, e.g., a charge-coupled device (CCD)) with 1-inch side length and 1024 x 1024 pixels (24.8 x 24.8 μm per pixel) that sits at 1-m effective focal length (EFL) behind the aperture—thus defining an angle of 1.455 degrees—will correspond to an area of 10000 x 10000 inches at 10 km or 254 x 254 m. In other words, 1 pixel on the FPA corresponds to an area of 0.248 x 0.248 m and thus the area S of 1 x 1 m will be imaged onto the FPA as 4 x 4 pixels (neglecting all other broadenings and blurrings).

Therefore the number of photons incident on each pixel is

3500 photons/sec/16 pixels $\approx$ 220 photons/sec/pixel

Typical objects reflect between 5 to 50% in the infrared between 1 to 2 μm (Reference 24), and the throughput of an optical system with interference filters for preselection of the wavelength range (< 50% transmission) and a Fabry-Perot (< 90% transmission at the bandpass) might be on the order of 10 to 30%. That reduces the number of photons received from the object S at 10-km distance to an order of magnitude of about 1 to 30 photons/sec/pixel.

A different scenario is based on a diffraction limited system with $\lambda/D \approx 1.6 \; \mu$m/0.30 m $\approx$ 5 μrad per pixel. At R = 10-km distance, each pixel would then subtend an area of $(R\lambda/D)^2 \approx (0.05 \text{ m})^2$ The target of 1 x 1 m would thus be imaged onto approximately 20 x 20 = 400 pixels and the number of incident photons per pixel and second would drop to 0.04 to 1.2.

Another question is how many photons the observer receives directly, without reflection from an object. A very similar calculation based on the above mentioned value of 430 γ/(sm^{2}arcsec^2) for the strongest OH line (again with the caveat that this is actually a fine structure double) finds that for the number of photons emitted into an angle of 5.12 x 5.12 arcsec (which corresponds to the solid angle maintained by 1 pixel in the above scenario), 820 photons/sec/pixel are received. Again, this should only be taken as an order of magnitude number.

Radiation Incident on a Specularly Reflecting Target

The target S of 1 x 1 m is again at 10-km distance from the observer. This is the second extreme case addressed. Ideal specular reflection is assumed, i.e., 100%. This time the contributing region of the OH layer is much smaller because the observer of the target will receive only the mirrored image of the light-emitting layer. Otherwise this is exactly the same calculation as in the last paragraph and the answer therefore is also that 820 photons are received per second and per pixel (N = 820 photons/sec/pixel).

WAVELENGTH COMPARISON

The previous calculations are based on the strongest available line at 1.66925 μm with an intensity of 430 γ/(sm^{2}arcsec^2). To detect images at this wavelength one would ideally employ an InGaAs detector array. Linear arrays of InGaAs were already available in 1996 with a quantum efficiency (QE) of 60% at 1.58 μm (Reference 25). In the meantime the QE has reached values of more than 80%.

However, if operation in a region accessible to Si-based CCD cameras is desired, suitable emissions in the region below 1000 nm need to be found (the wavelength range of Si-based detectors does not extend much beyond that). The strongest radiation there occurs very close to 1000 nm but the intensity (up to 60 R/Å) is quite reduced compared to the OH lines between 1500 to 1800 nm. The intensity in the lines between 1500 to 1800 nm can reach 2.3 kR/cm^{-1}, which together with the 3-cm^{-1} FWHM resolution results in 3 cm^{-1} 2.3 kR/cm^{-1} = 6.9 kR radiation. In the region < 1000 nm Broadfoot and Kendall's instrument had 5-Å FWHM resolution. The strongest line (Q band of 8 → 4 OH) at 9378 Å is listed with 60 R/Å, which results in 5 Å· 60 R/Å = 0.3 kR intensity, more than a factor of 20 difference. This line could also suffer from an atmospheric water band. In general, experiments measuring velocities of winds in the upper atmosphere, as described in the next section, have observation times on the 60-second scale or more.

TYPICAL OBSERVATION TIMES FOR ATMOSPHERIC WIND MEASUREMENTS

A short section on typical exposure times for atmospheric wind or airglow measurements is included here to enable comparison with other researchers' work.

Maihara and others (Reference 5) exposure of the HgCdTe 256 x 256 chip was 250 seconds per frame.

Broadfoot and Kendall's (Reference 8) total observational time for each section of 500 Å was about 2 to 3 hours. They used a scanning spectrometer with ca. 5-Å resolution and a datapoint recorded every 1.25 Å. That puts their recording time per datapoint in the neighborhood of 18 to 27 seconds.

Steed and Baker (Reference 10) employed time frames from 10 seconds to 1 minute using a field-widened interferometer. Total observation time for each of the two ranges was (measured with different detectors) about 10 minutes.

Bunn and Gush's (Reference 13) measurement time with an interferometer was 18 minutes per interferogram in 1970.

Sivjee and others (Reference 26) measured Doppler-broadened OI radiations using 5577 and 6300 Å of weak Aurotsl emissions using a low light level image orthicon TV camera coupled to a two-stage image intensifier. With an OI intensity of the 5577-Å line at 750 R "visually prominent TV images of the fringes were recorded in 0.5 second . . . ." "The TV camera produced fairly high quality real-time (1/60 sec) images of the circular Fabry-Perot rings from both [OI] 5577- and 6300-Å emissions originating from moderately bright aurora ($\approx$ 10 kR) at 5577 Å" (Reference 26 contains a misprint listing the source wavelength as 4477 Å). "Real-time fringe images from relatively weak emissions (< 1 kR), while visually discernible on the TV monitor, were less prominent . . . ." Their optical system contained two 15-cm diameter soft-coated etalons with a 1-cm spacer (free spectral range (FSR) 198 mÅ, finesse 11.7). They narrowed the incoming spectrum with bandpass prefilters 5- to 10-Å halfwidth. A f/8 objective achromat lens was also part of their system.

Rees and others (Reference 27) observed the P_1 (3) line of OH (coming from the 6 → 2 band) at 843 nm using an imaging Fabry-Perot interferometer (IFPI) at the Hardware Ranch Observatory near Bear Lake, Utah, 41.93°N, 11.42°W, 1970 m (6460 ft.) above sea level (Reference 27). According to them " . . . the average intensity of the OH (6 → 2) band Meinel mesospheric emission is around 400-600 R, with extreme variations between 100 and 1000 R." They state that " . . . the individual lines are weak (of order 100 R) and have been difficult to observe with traditional Fabry-Perot interferometers and detectors" (especially because of low QE). The clear aperture of their IFPI was 15 cm, the gap 20.49 mm, and " . . . designed in a way to overlap the lambda-doubled (6, 2) OH line at 843 nm." Their FPA device contained 256 x 256 pixels (no length data given). They detected typically 200000 signal photons per free spectral range during a 240-sec exposure, i.e., 0.0127 photon/sec/pixel (or about 3 photons/pixel in 240 sec). Of course only a small fraction of pixels will be illuminated. This must be compared to the intensity of the OH Meinel individual bands at 1500 to 1800 nm, which are about 50 times stronger than the line at 843 nm.

40

Doushkina and others (Reference 25) achieved a S/N = 1 at 1.7 kR/A photon flux. That corresponds to 4.3 kR/cm^{-1} for a S/N=1 only! They employed a bandpass filter centered at 1.5820 μm, which allowed observation from 1.5630 to 1.5820 μm. Their imaging lens had a 25-mm diameter (aperture of 4.9 cm^2) and a focal length f = 26.9 mm. Exposures were recorded with times of 4, 6, and 12 seconds but averaged over 5 minutes per spectrum (co-adding the exposures). The experiment started at sunset and continued for 80 minutes into the night. The actual spectrum shown was several kR/Å strong.

Coble and others (Reference 28) wrote in 1998 that " . . . Modern airglow imagers employ fish-eye lenses, narrow-band optical filters, and CCD detector arrays to obtain all-sky images of the airglow emissions. The most commonly used spectral range for OH imaging applications is 750-900 nm. When imaging the OH* Meinel bands, 60-s exposures are typical . . ." (Reference 29). They also mention the use of telecentric lenses to eliminate the angle dependence of the wavelength of the incoming light. Exposures have to be signal processed to get rid of star images and overexposures on the edge caused by the van Rhijn affect. The filters employed are broadband (e.g., 750 to 900 nm), sometimes notched to eliminate unwanted contributions, and at least in this case (Reference 28) not of the Fabry-Perot type.

SUMMARY AND RECOMMENDATIONS

In the first part of the Doppler velocimetry project using Fabry-Perot filtering, both active and passive approaches were explored.

One of the major results for the active approach is that long laser cavities with wavelengths in the blue range of the light spectrum are more advantageous when examining low speeds. This is based on the "overlap" speed $v_{overlap}$ necessary for a dynamic ring (reflected from the moving object) to overlap the next outer stationary fringe ring. The relevant equation is:

$$\frac{v_{overlap}}{c} = \frac{\Delta\sigma}{\sigma}$$

with c the speed of light, $\Delta\sigma$ the longitudinal mode spacing, and σ the wave number of the emitted laser light - $\sigma = 1/\lambda$ [cm^{-1}].

Comparing the intensities and photon fluxes it is found that even a low power Ar-ion laser (45-mW maximum) delivers photon numbers many orders of magnitude higher than the most promising natural sources.

The passive approach has explored the availability of natural spectral lines from 300 nm to about 10 μm. The most promising candidates in the night are lines emitted by OH molecules (OH Meinel bands) in the NIR part of the spectrum between 1500 to 1800 nm. These are much more intense than lines in the visible part of the spectrum; in fact the intensity generally increases with wavelength from 310 nm all the way to about 1800 nm. Based on the available literature they appear only to be Doppler broadened with temperatures of < 220 K and a FWHM of close to 0.04 Å. Their linewidth is the smallest available because the temperature of the emitting layer is –90°C. Other lines, e.g., the 5577-Å OI line, originate at higher altitudes and higher temperatures (more than 1000 K for the OI line) and are therefore more than twice as wide.

A FPA based on InGaAs technology capable of 80% quantum efficiency taking advantage of the much higher photon counts at 1600 nm should deliver a much better signal than a Si-based CCD camera working at around 900 nm, provided the noise figures (dark current, read out, etc) are comparable.

Potential candidates are at present:

- The **5577-Å OI spectral line with** $\approx$ **200 R** intensity, which would allow one to stay in the visible part of the spectrum.

- Other lines in the near infrared, e.g., the P_1 (3) line of the $6 \rightarrow 2$ OH Meinel band at 8430 Å—the corresponding Q-branch with a touch more intensity is at 8345 Å. Intensities are on the order of 100 R.

- The **9380-Å OH (8-4) Q1 Meinel line with** $\approx$ **300 R** intensity, which could still be used with Si-based CCD cameras but is impacted by a water band.

- **OH Meinel** lines in the NIR, e.g., **at 1.58334 μm or 1.66925 μm** with an intensity of $\approx$ **5000 R** or higher. For imaging purposes, this would require an InGaAs-based camera (there are other detectors in this wavelength range (PbS, PbSe), but their QE is not as good).

The first three of these appear to be quite weak compared to the OH Meinel bands between 1500 and 1800 nm, and at least the first two and maybe the third could be used together with an image intensifier. But even for those three the light levels appear low. In comparison, the intensities from the **laser light** (25-mW incident) were about 10^9 **R** (after reflection from the target) or **20·10^6 photons/(s m^2 arcsec^2)**, a factor of 10^5 difference. However, all of the mentioned lines are or were used to determine wind speeds of the upper mesosphere.

The recommendation of the report is to seek out a good imaging Fabry-Perot interferometer system presently in place, such as maybe the system used by Rees and others (Reference 27), copy it, and modify it for use at the OH Meinel lines between 1500 and 1800 nm. Such a system could then be tested imaging both stationary and moving scenery.

An alternative would be to use an OH Meinel band in a wavelength region accessible to an image intensified CCD (ICCD); their range does not extend to much more than 900 nm) and couple it to a low light level camera. There would be a tradeoff between QE of the detecting device and the strength of the line. The line at 9380 Å is stronger than the line at 8345 Å, but the improved QE of the ICCD detector at the shorter wavelength would more than make up for the difference.

One question that has not been addressed in the text is that the measured shift would be a convoluted signal of all contributing source directions. Because the source is extended, there is a whole range of scattering angles and thus a whole range of Doppler shifted wavelengths complicating an unambiguous deduction of the velocity.

In light of the previous paragraph, however, the chance for ultimate success of both approaches appears to be quite low. The amount of light available in the NIR region between 1500 and 1800 nm is much higher than that in the NIR from 800 to 1500 nm, and thus would be very useful for night vision purposes. But whether it is enough for a challenging application as the one presently explored remains to be seen.

REFERENCES

1. S. Gidon and G. Behar. "Instantaneous Velocity Field Measurements: Application to Shock Wave Studies," *Appl. Opt.,* Vol. 25 (1986), p. 1429.

2. S. Gidon and G. Behar. "Multiple-Line Laser Doppler Velocimetry," *Appl. Opt.,* Vol. 27 (1988), p. 2315.

3. G. Hernandez. "Measurement of Thermospheric Temperatures and Winds by Remote Fabry-Perot Spectrometry," *Opt. Eng.,* Vol. 19 (1980), p. 518.

4. Naval Air Warfare Center Weapons Division. Doppler Imaging With a Fabry-Perot Spectrometer and Laser, by L. Jones. China Lake, Calif., NAWCWD, 1998. (Internal report, report UNCLASSIFIED.)

5. T. Maihara, F. Iwamuro, T. Yamashita, D. N. B. Hall, L. L. Cowie, A. T. Tokunaga, and A. Pickles. "Observations of the OH Airglow Emission," *Pub. Astron. Soc. Pac.,* Vol. 105 (1993), p. 940.

6. Ch. Leinert, S. Bowyer, L. K. Haikala, M. S. Hanner, M. G. Hauser, A.-Ch. Levasseur-Regourd, I. Mann, K. Mattila, W. T. Reach, W. Schlosser, H. J. Staude, G. N. Toller, J. L. Weiland, J. L. Weinberg, and A. N. Witt. "The 1997 Reference of Diffuse Night Sky Brightness," *Astron. Astrophys. Suppl. Ser.,* Vol. 127 (1998), pp. 1-99.

7. E. I Reed and J. E. Blamont. *Space Res.,* Vol. VII (1967), p. 337 (referenced in Reference 6 above).

8. A. L. Broadfoot and K. R. Kendall. "The Airglow Spectrum, 3100 – 10,000 Å," *J. Geophys. Res.,* Vol. 73 (1968), p. 426.

9. D. J. Baker, and W. R. Pendleton, Jr. "Optical Radiation From the Atmosphere," in *Proc. SPIE ,* Vol. 91 (1976), p. 50.

10. A. J. Steed and D. J. Baker. "Night Sky Spectral Emission Measurements (λ 0.9 – 2.3 μm) Using a Field-Widened Interferometer-Spectrometer," *Appl. Opt.,* Vol. 18 (1979), p. 3386.

11. R. MacDonald, H. L. Buijs, and H. P. Gush. "Spectrum of the Night Airglow Between 3 and 4 Microns, " *Can. J. Phys.,* Vol. 46 (1968), p. 2575.

12. F. E. Bunn and H. P. Gush. "Spectrum of the Airglow Between 4 and 8 Microns," *Can. J. Phys.* , Vol. 48 (1970), p. 98.

13. S. Beckwith. "Star Formation and Techniques in Infrared and mm-Wave Astronomy," in *Lecture Notes in Physics 431*, ed. by T. R. Ray and S. V. W. Beckwith. Berlin, New York, Springer Verlag, 1994. P. 157.

14. D. J. Baker, A. J. Steed, and A. T. Stair, Jr. "Ground Observation of Resolved Hydroxyl ($\Delta v = 2$) Airglow," *J. Geophys. Res.*, Vol. 78 (1973), p. 8859.

15. J. W. Chamberlain. "Physics of the Aurora and Airglow," *Classics in Geophysics*, Washington, D.C., American Geophysical Union, 1995. P. 7.

16. F. G. Smith, ed. Atmospheric Propagation of Radiation, *The Infrared & Electro-Optical Systems Handbook*, Vol. 2, copublished by Ann Arbor, Michigan, Infrared Information Analysis Center, Environmental Research Institute of Michigan, and Bellingham, Washington, SPIE Optical Engineering Press, 2nd revised printing 1996.

17. P. J. Espy and M. R. Hammond. "Atmospheric Transmission Coefficients for Hydroxyl Rotational Lines Used in Rotational Temperature Determinations,"*J. Quant. Spectrosc. Radiat. Transfer*, Vol. 54 (1995), p. 879.

18. E. M. Dewan, W. Pendleton, N. Grossbard, and P. Espy. "Mesospheric OH Airglow Temperature Fluctuations: A Spectral Analysis," *Geophys. Res. Lett.,* Vol. 19 (1992), p. 597.

19. Gerhard Herzberg. "Einführung in die Molekülspektroskopie," Dr. Dietrich Steinkopff, Verlag, Darmstadt, 1973. P. 35.

20. M. C. Abrams, S. P. Davis, M. L. P. Rao, R. Engleman, Jr., and J. W. Brault. "High Resolution Fourier Transform Spectroscopy of the Meinel System of OH," *Astrophys. J. Suppl. Ser.*, Vol. 93 (1994), p. 351.

21. Department of the Navy. *The Infrared Handbook*, revised edition, ed. by W. L. Wolfe and G. J. Zissis, The Infrared Information and Analysis (IRIA) Center, Environmental Research Institute of Michigan, for the Office of Naval Research, DON, 1985. Chapter 3. (Publication UNCLASSIFIED.)

22. H. A. Gebbie, W. R. Harding, C. Hilsum, A. W. Pryce, and V. Roberts. "Atmospheric Transmission in the 1 to 14 µ Region," *Proc. Royal Society* , Vol. 206 A (1951), p. 87.

23. J. H. Taylor and H. W. Yates. "Atmospheric Transmission in the Infrared," *J. Opt. Soc. A.,* Vol. 47 (1957), p. 223.

24. J. L. Streete. "Infrared Measurements of Atmospheric Transmission at Sea Level," *Appl. Opt.,* Vol. 7 (1968), p. 1545.

25. V. V. Doushkina, R. H. Wiens, P. J. Thomas, R. N. Peterson, and G. G. Shepherd. "Spectral Imaging of O_2 Infrared Atmospheric Airglow With an InGaAs Array Detector," *Appl. Opt.,* Vol. 35 (1996), p. 6115.

26. G. G. Sivjee, T. J. Halinan, and G. R. Swenson. "Fabry-Perot Interferometer Imaging System for Thermospheric Temperature and Wind Measurements," *Appl. Opt.,* Vol. 19 (1980), p. 2206.

27. D. Rees, A. Aruliah, T. J. Fuller-Rowell, V. B. Wickwar, and R. J. Sica. "Winds in the Upper Mesosphere at Mid-Latitude: First Results Using an Imaging Fabry-Perot Interferometer," *Geophys. Res. Lett.,* Vol. 17 (1990), p. 1259.

28. M. R. Coble, G. C. Papen, and C. S. Gardner. "Computing Two-Dimensional Unambiguous Horizontal Wavenumber Spectra from OH Airglow Images," *IEEE Trans. Geoscience Remote Sensing,* Vol. 36 (1998), p. 368.

29. G. R. Swenson and S. B. Mende. "OH Emission and Gravity Waves (Including a Breaking Wave) in All-Sky Imagery From Bear Lake, Utah," *Geophys. Res. Lett.,* Vol. 21 (1994), p. 2239.

INITIAL DISTRIBUTION

2 Naval Air Systems Command, Patuxent River
    AIR-4.5.5.6
        M. Rankin (1)
        W. Scharpf (1)
1 Naval Sea Systems Command, Arlington (RADM M. Mathis)
3 Chief of Naval Research, Arlington
    ONR-351
        Chew (1)
        Siegel (1)
        Stachnik (1)
1 Naval Surface Warfare Center, Dahlgren (J. Bibel)
1 Naval War College, Newport (1E22, President)
1 Headquarters, 497 IG/INTW, Falls Church (OUWG Chairman)
2 Defense Technical Information Center, Fort Belvoir
1 Center for Naval Analyses, Alexandria, VA (Technical Library)

ON-SITE DISTRIBUTION

1 Code 4TB000D, J. Fischer
4 Code 4TL000D (3 plus Archives copy)
1 Code 4T4100D, C. Schwartz
3 Code 4T4110D
    S. Chesnut (2)
    L. DeSandre (1)
1 Code 4T4120D, C. D. Marrs
1 Code 452200D, R. Hintz